Geochemical proxies for water-soil interactions in the hyperarid Atacama Desert, Chile

Felix L. Arens[a*], Alessandro Airo[a], Jenny Feige[a], Christof Sager[a], Uwe Wiechert[b], and Dirk Schulze-Makuch[acd]

[a]Center for Astronomy & Astrophysics, Technische Universität Berlin, 10623 Berlin, Germany; [b]Department of Geochemistry, Freie Universität Berlin, 12249 Berlin, Germany; [c]German Research Centre for Geosciences (GFZ), Section Geomicrobiology, 14473 Potsdam, Germany; [d]Department of Experimental Limnology, Leibniz-Institute of Freshwater Ecology and Inland Fisheries (IGB), 12587 Stechlin, Germany

*Corresponding author, Hardenbergstraße 36A, 10623 Berlin, Germany, f.arens@tu-berlin.de

ABSTRACT

The Atacama Desert is the oldest and driest non-polar desert on Earth. Millions of years of hyperaridity enabled salt accumulations through atmospheric deposition. These salts can serve as proxies to decipher the interaction between water and soil as well as to understand the habitability with changing environmental settings. Therefore, we investigated four soil profiles regarding their mineralogy, salt abundance, and sulfate stable isotopic composition. The profiles were located along an elevation transect in the hyperarid region southeast of Antofagasta, Chile. The two lower sites situated on the distal parts of inactive alluvial fan deposits were subject to occasional fog occurrences. The upper steeper-sloped sites experienced no fog but are subject to minimal erosion. In all soil profiles, sulfates are the dominant salts showing a downward transition from gypsum to anhydrite that is accompanied by an increase of highly soluble salts and a decrease of sulfate $\delta^{34}S$ and $\delta^{18}O$ values. These trends are consistent with downward directed water infiltration during rare rain events causing salt dissolution followed by precipitation within the deeper soil column. This conclusion is also w supported by our Rayleigh fractionation model. We attribute the presence of anhydrite at > 40 cm depth to the cooccurrence of nitrate and chloride salts, which decreases water activity during sulfate precipitation and therefore drives anhydrite formation. Along the elevation transect, the total salt inventories of each profile show a trend for nitrates and chlorides concentration decreasing with elevation. This observation together with the sulfate stable isotopes indicates a fog-independent source and suggests remobilization of soluble salts through enhanced washout from hillslopes to alluvial fans. These findings are essential for assessing the long-term regional habitability of hyperarid environments and have also relevance for Mars.

Keywords: gypsum, anhydrite, stable isotopes, pedogenesis, hyperarid, Atacama Desert

1. INTRODUCTION

The core of the Atacama Desert (Fig. 1a) is currently hyperarid (mean annual precipitation <20 mm a^{-1}) and has been a desert for 12 ±1 Ma shifting between arid and hyperarid periods (Jordan et al., 2014). Accordingly, fluvial run-off is minimal and erosion rates are extremely low ranging from 0.2 to 0.4 m Ma^{-1} (Placzek et al., 2010). Under these circumstances, earthquakes, which are frequent in the region, contribute considerably to down-slope sediment transport through seismic shaking (Quade et al., 2012; May et al., 2019; Sager et al., 2020). Furthermore, the hyperarid conditions prevent the growth of vascular plants and keep the microbial biomass content at extremely low levels of $<10^{-6}$ cells g^{-1} soil in our study area (Schulze-Makuch et al., 2018), creating a carbon-limited environment (Azua-Bustos et al., 2017). Under these conditions, the soil CO_2 concentrations are too low for the formation of significant amounts of carbonates, which are commonly present in arid soils (Ewing et al., 2006). Hence, the Atacama Desert is of interest for studying the dry limits of life and has been used as an analog site for assessing the habitability on Mars (e.g., Warren-Rhodes et al., 2006; Azua-Bustos et al., 2018; Schulze-Makuch et al., 2018; Huang et al., 2020; Shen et al., 2020; Schulze-Makuch et al., 2021).

In contrast to arid deserts, precipitation in the hyperarid Atacama Desert is sufficiently low so that even the most soluble salts (e.g., chlorides, nitrates) are not entirely washed out but remain partially in the soil typically at depths of a few meters (Ericksen, 1981). Although many aspects on the origin, formation, and migration of these unique salt accumulations in the Atacama Desert are not fully understood, the following three sources of salts are assumed to dominate: (a) The groundwater in the Atacama Desert is recharged in the Andes mountains, carrying various ions depending on the substrate types (e.g., bedrocks, volcanic deposits, marine sediment) that have been leached during transport (Rech et al., 2003; Pérez-Fodich et al., 2014). The groundwater table is rarely close enough to the surface of the soils to be directly affected by its evaporation. However, at those locations, such as salars, where groundwater-related evaporites are formed they are readily redistributed regionally by aeolian processes (Rech et al., 2003). (b) Stratocumuli clouds developing over the Pacific Ocean carrying dissolved chloride and sulfate ions intercept with the Coastal Range and form advective fog that can migrate several tens of kilometers into the central parts of the hyperarid desert. However, fog migration is limited by the atmospheric inversion layer to altitudes below 1200 m above sea level (a.s.l.)

(Cereceda et al., 2008; Voigt et al., 2020). (c) Sulfate, nitrate, and perchlorate salts form in the atmosphere by lightning or photochemical reactions and are deposited regionally by dry fall (e.g., Michalski et al., 2004).

The formation conditions of various sulfate minerals found in the Atacama Desert are still under debate (Ewing et al., 2006; Voigt et al., 2020; Ritterbach and Becker, 2020). Laboratory experiments have shown that the temperature and water activity influence the hydration phases of $CaSO_4$, e.g., gypsum ($CaSO_4 \cdot 2H_2O$) and anhydrite ($CaSO_4$), the latter mineral being thermodynamically preferred at high temperatures and low water activities (Hardie, 1967). The metastable bassanite ($CaSO_4 \cdot 0.5H_2O$) can be formed by dehydration of gypsum at temperatures above ~80°C and low relative humidity (Seufert et al., 2009; Ritterbach and Becker, 2020). The hyperarid condition causes incomplete salt dissolution and limited migration into the soil, which has been shown to result in mass-dependent fractionation of sulfate $\delta^{34}S$ and $\delta^{18}O$ or chloride $\delta^{37}Cl$ isotopes with depth (Ewing et al., 2008; Amundson et al., 2012). This isotope fractionation depends on the net direction of the water flow and correspondingly, the inverse fractionation patterns were observed in the Atacama Desert at locations where groundwater evaporation dominates, such as salars (Finstad et al., 2016).

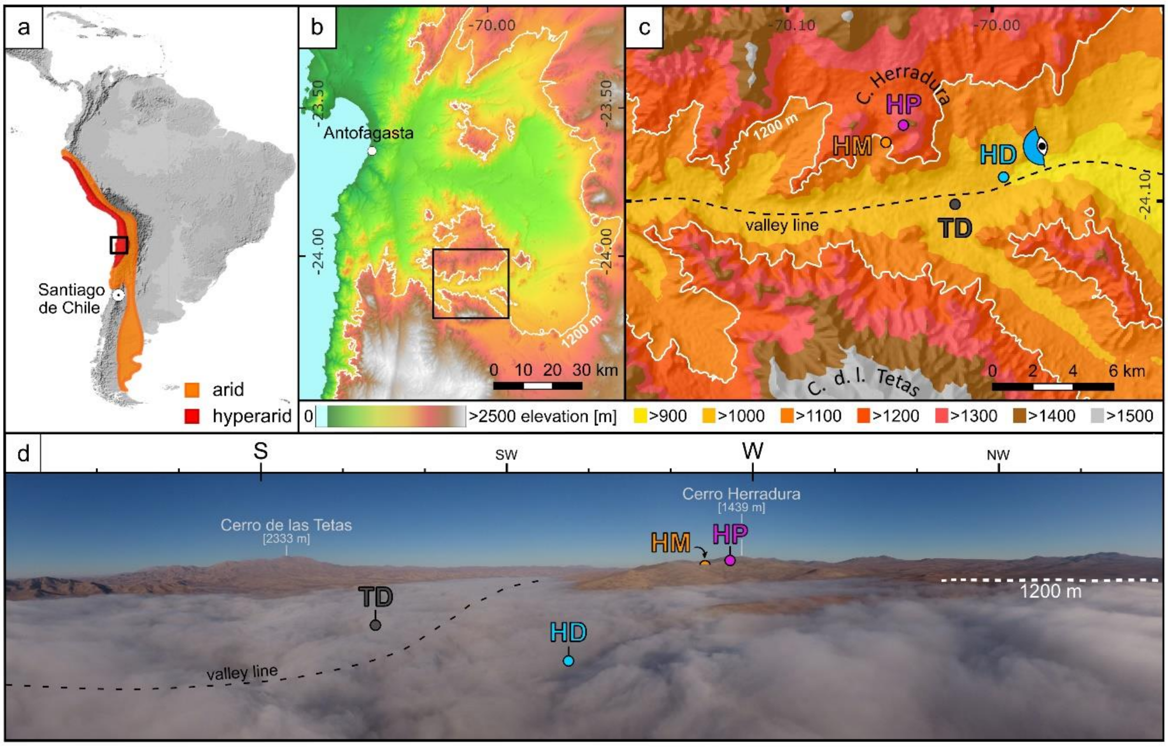

Figure 1 Location of study area. a) overview map shows arid and hyperarid regions in South America (after Houston and Hartley 2003), black rectangle indicates study region; b) topographic map of the study region located southeast of Antofagasta, in the southern part of the hyperarid core of the Atacama Desert (topography based on ASTER DEM (USGS)), the black rectangle shows the study area; c) topographic map of the study site in the Yungay valley: three sites (HP, HM,

HD) are located on the southern slopes of the mountain Cerro Herradura and one (TD) on the northern slopes of the mountain Cerro de las Tetas, eye symbol with indicated angle of view marks the position from which the photograph in d) was taken; d) panoramic photograph taken with an unmanned aerial vehicle at ~1400 m a.s.l. showing the studied valley, covered by fog on 9 August 2019 8:22 AM, reaching the 1200 m a.s.l. threshold. All elevation values refer to sea level (a.s.l.).

The prevalence of the extremely arid conditions for millions of years in association with an exceptional salt accumulation led to patterned grounds and the unique internal structuring of alluvial soils of the hyperarid Atacama Desert. These soils have been classified into five distinct horizons (Ericksen, 1981) described in the following. The upper 10 - 30 cm thick unconsolidated horizon (*chusca*), often fractured polygonal, consists of a desert pavement sitting on top of a loose, 1 - 5 cm thick layer of mainly sand- to clay-sized material that covers a brittle and porous 5 - 20 cm thick layer of vesicular texture largely composed of gypsum and anhydrite; referred to as 'vesicular layer' previously described by e.g., Owen *et al.* (2013). Frequently, on top of the vesicular layer, submerged in the loose material, are hand-palm-sized patty- to bowl-shaped ~5 cm thick aggregates of almost pure gypsum and anhydrite, called *losa*. The *chusca* transitions sharply into a moderately to firmly sulfate-cemented sandy to gravelly lithic sediment (*costra*). The *costra* is frequently polygonated by vertical sand wedges that partially extend through the entire horizon of roughly 2 m in thickness. The horizon below (*caliche*) is a firmly cemented nitrate-bearing layer of up to 5 m in thickness, which has been mined in the region for over a century. Further down lies either a salt-cemented regolith (*conjelo*) or a loose uncemented regolith (*coba*). Due to local variations in morphology and sedimentology the occurrence and development of these horizons can differ substantially. For this study we assumed that all soils are in equilibrium with the hyperarid conditions (i.e., gypsum-anhydrite & infiltration depth) that prevailed for millions of years. However, in the context of global climate change and the recent increase of precipitation in the region (Azua-Bustos et al. 2018), it is to be expected that the here described soil structures are subject to change. The aim of this study is to decipher the pedogenic processes acting under locally different environmental conditions by using the distribution, hydration phases, and isotopic fractionation of salts as geochemical proxies for the long-term interactions of water within the soils. Therefore, we describe and investigated four soil profiles along an elevation transect, which exhibits e.g., different erosion rates and exposure to fog.

2. SAMPLING AND METHODS

2.1. Study site selection and sampling

All investigated soils are located within a valley 60 km southeast of Antofagasta, a region commonly known as the ‘Yungay area’, which we here refer to as ‘Yungay valley’ (*Yungay* means “warm valley” in the Quechua language). The Yungay valley crosses the Coastal Cordillera from east to west and is confined by the mountains *Cerro Herradura* (1439 m a.s.l.) to the North and by the *Cerro de las Tetas* (2333 m a.s.l.) to the South (Fig. 1). Environmental data, collected over 4 years (1994-1998) in the area, show mean annual precipitation <2 mm a^{-1} and a mean annual temperature of +16 °C with a daily temperature range of ~20°C in the winter months and ~30°C in the summer months (McKay et al., 2003). In our study region rain originates in the southwest over the Pacific Ocean (Houston and Hartley, 2003) and is favored during El Niño years with increased sea surface temperature in the eastern tropical Pacific (Bozkurt et al., 2016). This was the case in the most recent rain event previous to our sampling in March 2015 (Jordan et al., 2015; Bozkurt et al., 2016). Over 30 mm of total rain caused soil moistening over months, as well as surface overland run-off on hillslopes, subsurface flow, and change in soil mineralogy in our study region (Jordan et al. 2020; Pfeiffer et al., 2021). This rain event was followed by a rain event with a similar magnitude in 2017, which is discussed as a consequence of global climate change (Azua-Bustos et al., 2018). Furthermore, fog is a more frequent water source in the Yungay valley but being limited to <1200 m a.s.l., which was also observed by us during the 2018 and 2019 field campaign (Fig. 1d). Groundwater evaporation affecting the soils in the Yungay valley is unlikely because an abandoned mining well nearby was dry down to 40 m depth, and even the lower elevated Salar Aguas Blancas (961 m a.s.l), 10 km to the east of the study area, is currently not connected to the groundwater aquifers (Artieda et al., 2015). Our four sampling locations were selected for sampling along an elevation transect ranging from lower fog affected sites to higher non-fog affected terrain. Three study sites are located on the south-facing slope the *Cerro Herradura*, which are referred to as: Herradura Proximal (HP) (1436 m a.s.l.), located close to the top of the mountain; Herradura Medial (HM) (1217 m a.s.l.) located on the upper mountain slope; and Herradura Distal (HD) (1005 m a.s.l.), located on the lower mountain slope. The fourth site, Tetas Distal (TD) (1021 m a.s.l.), was located on the lower north-facing slope of the *Cerro de las Tetas* (Fig. 1; Tab. S1). The two lower sites (HD, TD) have been investigated previously and the pits were still accessible (HD: Schulze-Makuch et al., 2018; TD: Ewing et al., 2006, 2008; Sutter et al., 2007; Wilhelm et al., 2017). The HD profile as well as the topmost 140 cm of the TD profile corresponds to the hyperarid soil described by Ericksen (1981), while the sediments below have been dated by argon isotope ratio of an ash layer, showing that they are older than 2 Ma and presumably formed under more humid conditions (Ewing et al., 2006). It was also shown that the upper soil layers are volumetric increasing due to atmospheric salt and dust deposition and minimal fluvial erosion (Ewing et al., 2006). Furthermore, a downward decrease of $\delta^{34}S$ and $\delta^{18}O$ was observed, indicating an in-soil fractionation of sulfate S and O isotopes due to downward directed meteoric water infiltration (Ewing et al., 2008). These preexisting pits were excavated laterally > 30 cm to obtain fresh samples, which have been analyzed for this study.

The other two pits, selected to be at elevations above (HP) or close to (HM) the upper fog-boundary (~1200 m a.s.l.), were excavated for this study during a field campaign in 2017. Soil samples were collected with a hand shovel and a spatula at increments of 10 cm down to at least 1 m depth for each pit. The exact sampling positions were chosen to represent the typical soil at each depth interval, especially avoiding the sampling of the sand wedges.

2.2. X-ray diffraction (XRD)

Pristine soil samples were homogenized and ground manually to powder for analyzing the bulk salt mineralogy. XRD analysis of crushed soil samples was performed by using a powder diffractometer *Empyrean* (Malvern Panalytical, Netherlands), at the Laboratory of Mineralogy at the Freie Universität Berlin, performing step scanning with a strip detector measuring 255 steps simultaneously. The X-ray source is a Cu Kα radiation (K-alpha1= 1.540598 Å, K-alpha2=1.54439 Å) with a performance of 40 kV and 40 mA. A step interval of 0.013° 2Θ with a step-counting time of 20 s was used in a scanning range from 10° to 90° 2Θ. Finally, a semi-quantitative evaluation of all the results was conducted with the software *High Score* (Malvern Panalytical, Netherlands) and the *PDF-2* (International Center for Diffraction Data, USA) database.

2.3. Soluble weight loss

50 to 150 g of pristine soil, depending on maximum grain size and cementation, was leached in two steps to determine the weight percent (wt%) of soluble salts in each sample. In the first step, one-liter deionized water was used to leach the highly soluble salts and in the second leaching procedure with multiple sequential leaching steps, 0.2 molar hydrochloric acid (HCl) was added in amounts sufficient for a complete dissolution of all salts including sulfates. To ensure this, 2 ml leachate of each step was evaporated and checked for visible precipitants. Afterwards the samples were dried and weighed again for determining the weight loss related to the soluble fraction. Repeated measurements gave a reproductivity of <5% (n = 3) variation.

2.4. Ion chromatography

The leachates of the above-described method for soluble weight loss were used to determine the concentration of sulfate (SO_4^{-2}), chloride (Cl^-) and nitrate (NO_3^-). Cl^- and NO_3^- concentrations were solely determined on the water leachate. SO_4^{-2} was determined on water leachate and the pooled HCl leachate, measured separately, and corrected for the leachate solution quantity. The analysis was conducted by using capillary electrophoresis (CE) chromatography *3D CE G1600A* (Hewlett-Packard, USA) at the Department of Soil Science of the Technische Universität Berlin. Carbonate ions are lost due to CO_2-degassing and therefore carbonates cannot be measured with this method. Performing the procedure several times on the same sample yields a variation in reproducibility of <10% (n=3).

2.5. Stable isotope analysis

Isotope ratios measurements of sulfur and oxygen were performed on sulfates. The isotope-ratio of ^{34}S and ^{32}S ($\delta^{34}S$) are related to Vienna Canyon Diablo Troilite (VCDT) and ^{18}O and ^{16}O ($\delta^{18}O$) are related to Vienna Standard Mean Ocean Water (VSMOW). Therefore, the water- and HCl-leachates of each sample were pooled under consideration of the leached volume. Barium chloride was added to precipitate barium sulfate ($BaSO_4$). The precipitate was filtered, rinsed with Millipore water and dried at 70°C for 3 days. Samples duplicates were weighed into tin capsules and vanadium pentoxide (V_2O_5) was added as a catalyst for $\delta^{34}S$ analysis. These capsules were combusted in a furnace operating at 1000°C with O_2 using a gas chromatograph, which separates SO_2 from other combustion products. The pure SO_2 was then measured for the $\delta^{34}S$ values. For $\delta^{18}O$ analysis, solely $BaSO_4$ precipitate of taken samples was weighed within silver capsules. Sulfate oxygen was converted to CO by pyrolysis at 1400 °C. The $\delta^{34}S$ and $\delta^{18}O$ measurements were performed with a mass spectrometer *MAT-253* (Thermo Fisher Scientific, USA) combined with a Eurovector elemental analyzer (HEKAtech, Germany) at the Institute of Geological Sciences, Freie Universität Berlin. The measured isotope values $\delta^{34}S$ and $\delta^{18}O$ were corrected and standardized based on in-house sulfate (K_2SO_4) standard and international sulfate ($BaSO_4$) standards NBS-127, IAEA-SO5 and -SO6 and sulfide (Ag_2S) IAEA-S-1 and -2. Reproducibility of the analyses is ±0.3‰ (2SD) for $\delta^{34}S$ and ±0.6‰ (2SD) for $\delta^{18}O$.

2.6. Rayleigh fractionation model

We applied the Rayleigh fractionation model, as described by Criss (1999), to derive the fractionation effects for the case of downward migration of sulfate solutions. The model describes the water transport and precipitation of sulfate in each layer, which increases $\delta^{34}S$ and $\delta^{18}O$ in the solid fraction compared to the remaining dissolved fraction. Hence, for $\delta^{34}S$ (and similarly for $\delta^{18}O$) in the dissolved (d) and the cumulative solid (s) fractions at depth z the Rayleigh model in δ notation states that

$$\delta_d{}^{34}S\,(z) = \left(\delta_{d,0}{}^{34}S\,(z) + 1000\right) f^{\alpha-1} - 1000\ [‰], \tag{1}$$

$$\delta_s{}^{34}S\,(z) = \left(\delta_{d,0}{}^{34}S\,(z) + 1000\right) \frac{1-f^{\alpha}}{1-f} - 1000\ [‰]. \tag{2}$$

Equation (2) was derived from the mass balance equation

$$\left(f_s(z) + f_d(z)\right) \delta_{d,0}{}^{34}S\,(z) = f_d(z)\delta_d{}^{34}S\,(z) + f_s(z)\delta_s{}^{34}S\,(z), \tag{3}$$

by inserting $\delta_d(z)$ from equation (1) into equation (3) and rearranging results. The dimensionless isotopic fractionation factor α is defined as the ratio of the isotope ratios in the heavy (solid) to the light (dissolved) fraction, i.e. $\alpha > 1$, and which is related to the isotope enrichment factor ε (in ‰) by

$$\alpha = \frac{\epsilon}{1000} + 1. \tag{4}$$

The process variable f in layer z is defined as the ratio of the dissolved fraction f_d remaining after precipitation to its total inventory,

$$f(z) = \frac{f_d(z)}{f_d(z) + f_s(z)}, \tag{5}$$

where $f_s(z)$ is the layer-thickness (d)-weighted and normalized solid fraction measured in layer z,

$$f_s(z) = \frac{d(z)SO_4^{2-}(z)}{\sum_z d(z)SO_4^{2-}(z)}, \tag{6}$$

with SO_4^{2-} being the sulfate concentrations in mg g^{-1}, and

$$f_d(z) = f_d(z-1) - f_s(z). \tag{7}$$

We used isotope enrichment factors $\varepsilon_S = 2.0$ ‰ for sulfur and $\varepsilon_O = 3.3$ ‰ for oxygen (Van Driessche et al., 2016). We assumed that at the beginning of the Rayleigh process the entire reservoir was present in dissolved form, hence $f = f_d = 1$. In order to derive the initial values for $\delta_{d,0}{}^{34}S$ (and similarly for $\delta_{d,0}{}^{18}O$) in the topmost layer, we calculate the layer-thickness- and concentration-averaged mean value from all layers, with

$$\delta_{d,0}{}^{34}S = \frac{\sum_z d(z) \times SO_4(z) \times \delta_{sample}{}^{34}S}{\sum_z d(z) \times SO_4(z)} \ [‰], \tag{8}$$

where $\delta_{sample}{}^{34}S$ are the measured values, and $SO_4^{2-}(z)$ the measured concentrations. The corresponding δ-values for layers z below the topmost layer were calculated with equation (1) and further used as input for z+1, e.g. $\delta_d{}^{34}S(z) = \delta_{d,0}{}^{34}S(z+1)$.

3. RESULTS

The investigated soils lie on slopes between 1005 and 1436 m a.s.l., increasing in steepness from distal (HD, TD) to proximal (HP) in relation to the sediment source (Fig. 2a; Table S1). Weighted average stable isotope values for each soil profile were calculated considering the sampling-interval and the sulfate content (Fig. 2b). It shows that the highest elevated soil (HP) compared to the lowest (HD) contain sulfates with 2.3‰ higher $\delta^{34}S$ values and 2.6‰ lower $\delta^{18}O$ values. Comparing the soils within a similar elevation on the Cerro de las Tetas slope (TD) with the Cerro Herradura slope (HD) indicates variability in $\delta^{34}S$ values of 1.5‰ and $\delta^{18}O$ values of 2‰, respectively. These relations of the average isotope values are consistent, independent of the considered soil depth (Fig. S2). Figure 2c presents the total anion inventory for each soil profile, calculated for a soil column with a surface area of 1 m² and an estimated bulk soil density of 1000 kg m^{-3}. All soils accumulated high amounts of sulfates (>200 kg m^{-2}), showing signs of salt-heave and -shattering, resulting in siliciclastic clasts embedded within a sulfate-dominated matrix (e.g., Fig. S3b). Figure 3a shows the schematic build-up of all four soil profiles. The two soils at highest elevation (HP, HM) shift at around 1 m depth into either unweathered shattered bedrock fragments of a few mm in diameter (HP) (Fig. S2), or into large unweathered and angular intrusive rock-fragments (HM) (Fig. S3). Fluvial run-off occurs predominantly on steep hillslopes, which recently has been recorded during heavy rain events in 2015 and 2017. During these events, new run-off incisions and small debris flows on the slopes of Cerro Herradura formed (Fig. S4). The other two soils residing on top of inactive alluvial fans do not show sedimentary indications of fluvial transport. However, they contain mostly well-rounded partially chemically weathered clasts deriving from the alluvial deposits and partially embedded within a sulfate cemented matrix (Fig. S5). At the TD site, the sediments below 1.4 m depth graduate into fine-grained calcite-cemented paleosol containing plant remains (Fig. S6).

A commonality to all soil surfaces is the 10 - 30 cm thick *chusca* horizon (Fig. 3c; Fig. S3c). *Losas* are embedded within the *chusca* (Fig. S7), can contain small amounts of anhydrite (Fig. 3). They are absent at HP and only moderately developed at HM, but are ubiquitous and largest in size at the two lower sites (HD, TD). The same trend applies to the degree of ground patterning, which is characterized by soil segmentation into sulfate-cemented polygons of a few meters in diameter. These polygons are separated by downward-narrowing wedges of poorly cemented and vertically layered sediments (Fig. 3; Fig. S5, S6). While polygonation is absent at HP, these wedges become wider and deeper with decreasing site-elevation and reach down to the *costra* or *caliche* horizons at HD and TD, respectively.

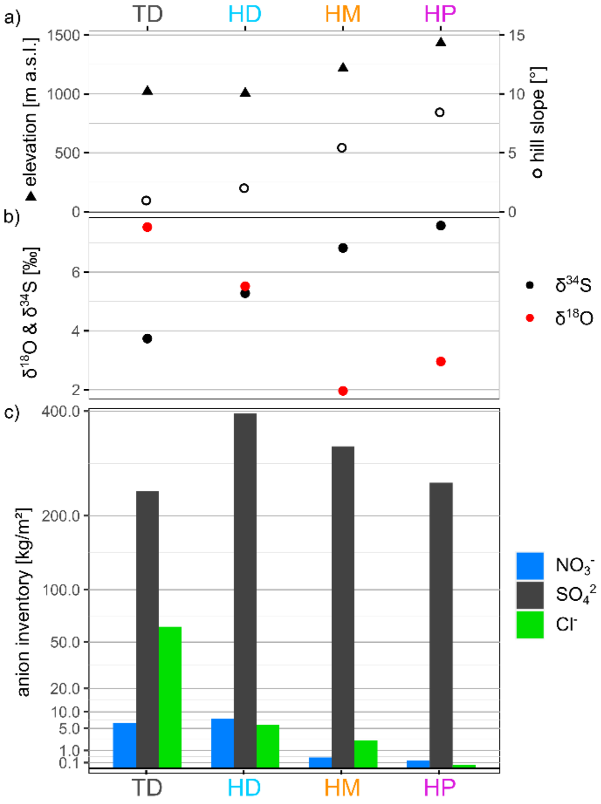

Figure 2 Bulk comparison for each soil profile (Tab. S1). a) elevation and hill slope; b) total weighted average sulfate $\delta^{34}S$ and $\delta^{18}O$ (For TD only values down to 112 cm depth from Ewing et al. (2008) are considered, as values below are inconsistent). These trends with soils depth are corroborated in the supplement (Fig. S1); c) total nitrate, sulfate, and chloride inventory, except for TD where only values <140 cm depth are considered.

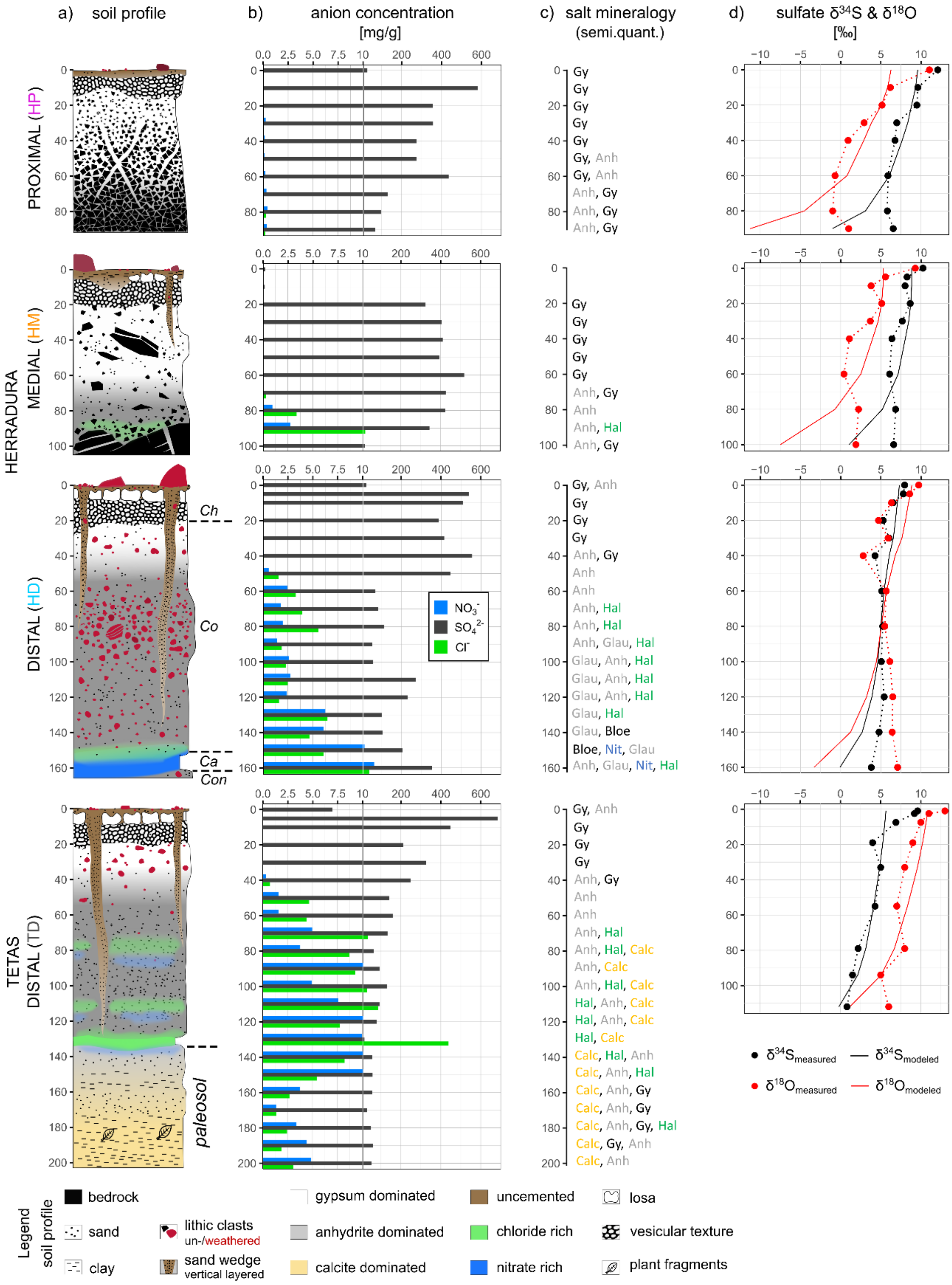

Figure 3 Geochemical results for each soil profile, depth in cm (Tab. S2). a) profile sketch (Ch = chusca, Co=costra, Ca=caliche, Con=conjelo); b) anion concentration of SO_4^{2-}, Cl^-, NO_3^- vertical axis scale changes at 20mg g^{-1} to visualize low and high concentrations; c) salt mineralogy by XRD, starting from the most abundant to minor fraction Gy = gypsum; Anh = anhydrite; Hal = halite; Glau = glauberite; Bloe = bloedite; Nit = nitratine; calc = calcite; d) sulfate $\delta^{18}O$ & $\delta^{34}S$

values, measured and modeled applying a Rayleigh equation (Criss, 1999) using fractionation factors from Van Driessche et al. (2016). Isotopic data from TD are from Ewing et al. (2008).

The concentrations of chlorides and nitrates along the investigated transect generally decrease from low to high elevations (Fig. 2c, Tab. S1). Within each soil profile, the chlorides and nitrates are concentrated at depth below 40 – 60 cm. However, we do not observe a significant correlation between total soil sulfate concentration and site elevation (Fig. 2c). Sulfates are the most abundant salt in all soils but show an overall downward decrease in amount. Within each soil profile, sulfate concentrations are the highest in the *chusca* horizon occurring in the form of the vesicular layer (gypsum) and if present also as *losas* (gypsum and minor anhydrite) (Fig. 3b, c). In the lower part of the HD profile, highly soluble sulfates (glauberite and bloedite) accumulate, following the trend of a downward increase in concentrations of the more soluble salts (Fig. 3c). Within the *costra* horizon, gypsum transitions consistently into anhydrite below half a meter depth. The anhydrite detected by XRD was exclusively anhydrite-II (if not mentioned otherwise, we use the term ‘anhydrite’ synonymously for ‘anhydrite-II’).

Our stable isotope data for the profiles HP, HM, and HD shows an overall decrease in $\delta^{34}S$ and $\delta^{18}O$ values with depth, being most prominent within the first half meter; an observation made previously by Ewing *et al.* (2008) for the TD profile (Fig. 3d). Applying our Rayleigh model with a downward water flow results in a similar trend as the measured values (Tab. S2), while modeling the inverse water flow results in an anti-correlation in comparison with the measured values (Fig. S8).

4. DISCUSSION

4.1. Elevation-related soil attributes

The HD and TD soil profiles located on inactive alluvial fan deposits correspond well to the hyperarid soil type described by Ericksen (1981). Due to the gentle slope and porous *chusca* horizon surface, rainwater usually infiltrates entirely into the subsurface (Pfeiffer et al., 2021; Sager et al., 2021). As a result of minimal erosion, the accumulation of salts results in a net deposition (Ewing et al., 2006). The two upper soils (HP, HM) are less mature, exhibiting only little developed polygons and little to no *losas*. Furthermore, the rapid transition into poorly weathered bedrock and the occasional fluvial run-off on higher elevated steeper sloped surfaces is consistent with these sites being subject to net erosion as proposed previously (Placzek et al., 2010). However, the erosional rates are sufficiently low for allowing the accumulation of substantial amounts of salts through atmospheric deposition, mainly sulfates. Although the absence of the surface-near *losas* at the HP site might reflect an elevated erosion rate, we cannot exclude that their formation required frequent moisturization by fog, which does not reach the upper sites. The sulfate-rich vesicular layer is ubiquitous in the study area and of a similar extent at all sites (Fig. 3a), indicating a relatively rapid formation independent of elevation and sedimentary setting. These observations are consistent with a formation mechanism of the vesicular layer mediated through repetitive eolian input of clays and salts as well as little rainwater infiltration and evaporation; a formation process also proposed for the analogous carbonate-rich vesicular layer found in the arid soils of the Mojave Desert, North America (McFadden et al., 1998; Anderson et al., 2002). In the case of the hyperarid Atacama Desert the cooccurring salt dissolution and reprecipitation, as well as hydration and dehydration of sulfates can play an important role in the formation of vesicular structure (Pfeiffer et al., 2021).

Furthermore, both upper profiles (HP, HM) contain fewer amounts of the highly soluble nitrates and chlorides (Fig. 2c), even though we cannot preclude a higher abundance of nitrates and chlorides at greater depth. However, we assume this not to be the case because of the rapidly decreasing total salt content and pore space at both sites. Consequently, the lower amounts of these salts can be either due to lower input or higher output rates. Nitrates, which are formed in the atmosphere (Michalski et al., 2004; Ewing et al., 2007) and assumed to be initially deposited homogeneously without significant elevation-dependent input rate variations, would therefore need to be subject to higher output rates at the upper sites. In contrast, the major sources of chlorides in the region are basin-associated salars connected to the groundwater (Pérez-Fodich et al., 2014) and ocean-derived fog (Voigt et al., 2020). Thus, we cannot exclude that the decrease in chlorides with increasing elevation is related to lower input rates. We conclude that downslope aqueous wash-out and a subsurface migration are responsible for the lower concentrations of nitrates and perhaps also chlorides in the upper soils (HP, HM) in comparison to the lower soils (HD, TD) (Fig. 4). Over time, the highly soluble salts accumulate within the flat alluvial fans, which, under more humid climate conditions, would be washed out or in the case of nitrates could be metabolized by microorganisms. The less soluble sulfates are similarly abundant in all four soils indicating that the little precipitation is only able to wash-out and transport downhill the most soluble salts.

The weighted average δ^{34}S values of all the sulfates present within each of the four soil profiles range from 3.7 to 7.6‰ (Fig. 2b), indicate a dominantly volcanic sulfur source (0 – 5‰) (Rech et al., 2003). The values from the higher elevated sites (HP, HM) being slightly above the volcanic isotope values points to an additional source of heavier sulfur. Although marine-derived fog contains heavy sulfates (δ^{34}S ~ 21 ‰), we consider this source to be irrelevant, since the fog only reaches the lower sites (HD, TD). However, we cannot exclude that the pattern of fog migration has changed through time. Alternatively, it is conceivable that beyond the in-soil vertical isotopic fractionation a long-distance downslope isotopic fractionation occurred over geological timescales. Contrary to the δ^{34}S values, the weighted average δ^{18}O values, ranging from 2.0 to 7.5 ‰, are lower at the higher elevated sites (HP, HM). The higher δ^{18}O values at the lower sites (HD, TD) could indicate an exchange of oxygen between sulfate and water, a process that causes strong isotopic fractionation of up to 31‰ but occurs at a slow rate of 10^5 years at 25°C (Lloyd, 1968; Zeebe, 2010). We assume that the lower sites (HD, TD) are subject to longer wetting periods, because of their larger catchment area and enhanced infiltration capacity. This would explain why they exhibit higher δ^{18}O values compared to the upper sites (HP, HM). However, these elevation-dependent isotopic trends and their causes warrant further investigation.

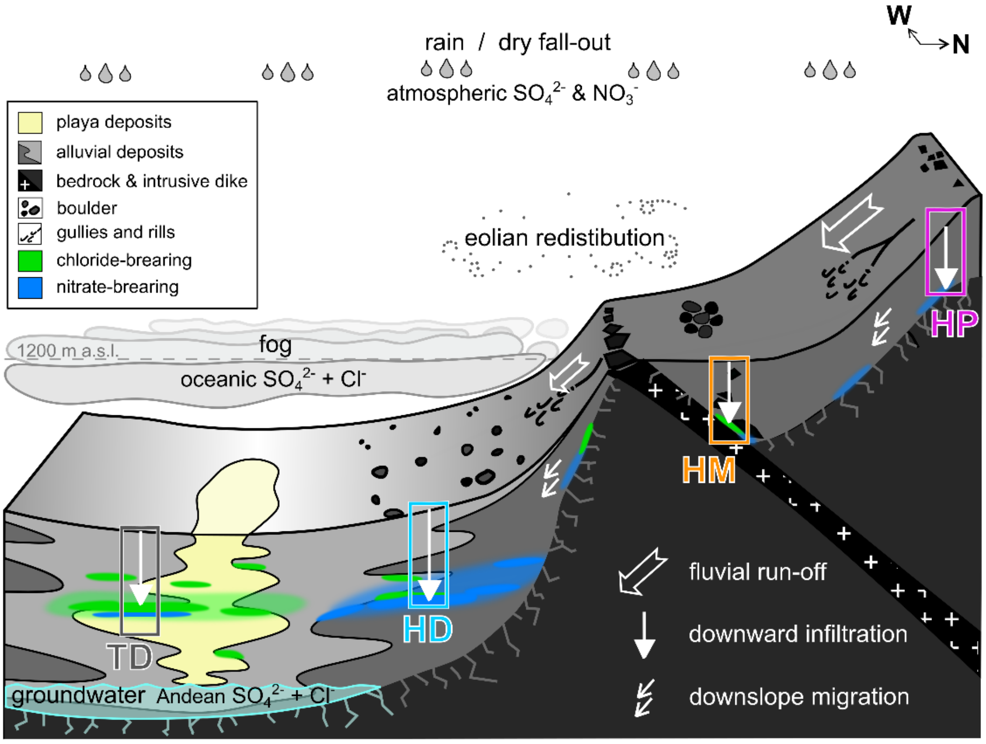

Figure 4 Sketch of salt input and distribution within the Yungay Valley. SO$_4^{2-}$ and NO$_3^-$ are brought into the system homogeneous by dry fall-out, eolian dust, or rain. Cl$^-$ is more limited to lower elevation as the source is mainly the ocean, distributed by fog and eolian dust or saline groundwater, also redistributed by eolian dust. Once in the soil, salts can be redistributed again. Rare rain events lead to downward in-soil salt transport. However, there are indications on rare fluvial run-off and downslope transport, due to steeper hill slopes at HP and HM. All three transport mechanisms lead to incomplete leaching of the salts, causing a fractionation of salts by solubility, within the soil column as well as along the investigated transect.

4.2. Water-soil interactions

Our individual soil profile data indicates that water-soil interactions in our study area are dominated by short-distance downward rainwater infiltration, independent of elevation and sedimentological setting. The downward increase of the salt solubility reflects the dominant direction and reach of water flow since the Pleistocene (Ewing et al., 2006). Furthermore, all profiles show a systematic decrease of $\delta^{34}S$ and $\delta^{18}O$ sulfate values to at least a depth of 40 cm, as was observed by Ewing *et al.* (2008) for the TD profile, which is consistent with a Rayleigh fractionation resulting from sulfate precipitating out of downward migrating water.

Although, the modeled and measured $\delta^{34}S$ and $\delta^{18}O$ data show a similar downward trend of decreasing values, we find the following two main deviations: (1) Within the upper half meter the measured values decrease more rapidly than the modeled data. (2) Below half a meter the measured values decrease only a little or even increase with depth. These discrepancies indicate that the here used simple Rayleigh model can only replicate the general trend of isotopic distribution within the soils. Hence, the processes controlling isotope fractionation in the natural environment are more complex and could include the following aspects: the presence of soluble salts in the lower soil layers elevates the salinity during $CaSO_4$ precipitation, which is known to influence isotope fractionation (Van Driessche et al., 2016). The porous and permeable *chusca* horizon is most frequently exposed to meteoric water and therefore is the most dynamic horizon, which could explain why measured isotopic fractionation is stronger than seen in the modeled data. This upper soil horizon is also affected by salt efflorescence after rain events and through artificial rain experiments (Sager et al., 2021, Pfeiffer et al., 2021), which indicates more complex water pathways at the surface than dominant downward migration, influencing potentially also the isotopic fractionation. Furthermore, rainwater infiltration is not homogeneous and is most intense along the sand wedges (Owen et al., 2013), presumably affecting the lateral isotope pattern. The deviation of the modeled versus measured data in the lower soil layers, especially the bottom value, likely relates to sulfate migration not terminating at the bottom of the considered depth as assumed in our model.

Under ideal conditions isotope fractionation of a single sulfate source should result in a systematic correlation of the $\delta^{34}S$ and $\delta^{18}O$ values that reflect the ratio of the enrichment factors ($\varepsilon_O/\varepsilon_S = 1.7 \pm 0.3‰$) (Van Driessche et al., 2016). Fig. 5 shows the correlation between $\delta^{34}S$ and $\delta^{18}O$ values and their coefficient of determination (R^2) for each soil profile. Additionally, this data was divided into the upper 50 cm, which is dominated by gypsum and the lower section, which is dominated by anhydrite and the occurrence of more soluble salts. This correlation is highly significant for the upper profiles HP and HM with R^2 values >0.9 independent of the considered soil depth. Equally significant is the correlation for the upper 50 cm of the HD profile, while the lower section shows an inverse correlation with an R^2 value of 0.51. At the TD site from Ewing *et al.* (2008) the correlation is moderately independent of the considered soil depth.

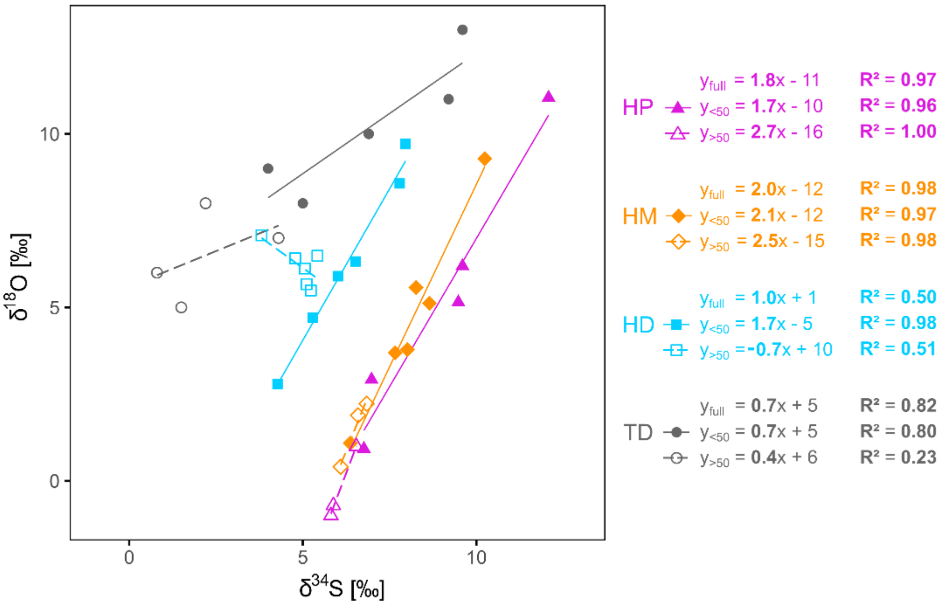

Figure 5 Correlation between $\delta^{34}S$ and $\delta^{18}O$ for each soil profile. Values for TD site from Ewing et al. (2008). The linear regressions are plotted for the values above (solid/filled) and below (dashed/void) 50 cm depth. The equations for the linear regressions as well as the corresponding coefficient of determination R^2 are given for each profile: entire profile (y_{full}), values above 50 cm depth ($y_{<50}$), and values below 50 cm depth ($y_{>50}$).

The values of the two upper soil profiles (HP, HM) follow this trend (i.e., the slope) with high significance independently of the considered soil depth (Fig. 5). This supports the assumption that these soils have only a single sulfate source entering from the top, which is consistent with an erosive soil.

Although we find the same systematic correlations of the $\delta^{34}S$ and $\delta^{18}O$ values at the HD site in the upper half meter, below we observe an anticorrelation between the $\delta^{34}S$ and $\delta^{18}O$ values. This change in isotope pattern might result from a change in fractionation due to the presence of highly soluble sulfates (in the case of HD glauberite and bloedite), which presumably have a different fractionation factor (Seal et al., 2000) or it could be due to long-term oxygen exchange with water causing an isotopic fractionation as described in section 4.1. At the TD site the correlations of the $\delta^{34}S$ and $\delta^{18}O$ values are slightly lower (R^2 ~0.8) and have a different $\varepsilon_O/\varepsilon_S$ value of 0.7 (Fig. 5). This difference might be due to the varying sediment source (Cerro de las Tetas) and/or resulted from the interaction with ground water in the past (>2 Ma) during arid conditions.

4.3. Gypsum vs. anhydrite

The occurrence of anhydrite in the region has been interpreted as an indicator for long-term hyperaridity (Ewing et al., 2006; Voigt et al., 2020). Ewing *et al.* (2006) have interpreted that the lower anhydrite-dominated soil at the TD site is caused by the low mean soil relative humidity, reported to be only 20 % (Warren-Rhodes et al., 2006), while the upper gypsum-dominated soil is subject to enhanced and more frequent wetting and hydration. More recently, Voigt *et al.* (2020) have shown in the Atacama Desert a correlation between the regional aridity and the occurrences of anhydrite and gypsum within surface-near soils (< 40 cm depth) located between 25°S and 19°S latitudes, where anhydrite dominated in the northern, most arid regions. Other studies have found a shift of hydration phases of near-surface calcium sulfates after the extreme rain event in 2015 (e.g., Schulze-Makuch et al., 2018; Pfeiffer et al., 2021). Considering the proposed dehydration of gypsum after a rain event by high surface temperatures reaching 60°C, Pfeiffer *et al.* (2021) concluded that the uppermost *chusca* horizon is subject to rapid dehydration-hydration cycles. In the context of our findings, we propose that the formation of anhydrite within the shallow *chusca* horizon relies on high temperatures, while the systematic transition from gypsum to anhydrite within the *costra* horizon at ~50 cm depth (Fig. 3c) is related to the presence of nitrates and/or chlorides and only indirectly linked to aridity. The interrelation is based on the following reasons:

Initial atmospheric sulfate deposition is dominated by gypsum because anhydrite formation is kinetically hindered under conditions of rapid rainwater evaporation (Freyer and Voigt, 2003). Thus, the gypsum-anhydrite transformation must occur post-depositional through either dry dehydration or gypsum-dissolution followed by slow anhydrite-crystallization. Laboratory experiments, performed over several months, could only show dry dehydration of gypsum to occur above 85°C forming bassanite ($CaSO_4 \cdot 0.5H_2O$) and anhydrite-III ($CaSO_4$) (Seufert et al., 2009). A more recent study from Ritterbach and Becker (2020) could demonstrate that the dehydration of gypsum to bassanite can occur already at 76°C for an experiment duration of 60 h. However, such high temperatures do not typically occur in our study region (McKay et al., 2003) and we did not detect any bassanite or anhydrite-III within the *chusca*, which lets us conclude that dry dehydration does not play a significant role in the formation of anhydrite. However, the formation of anhydrite from a saturated $CaSO_4$ solution through slow precipitation can occur already at temperatures above 42 ±2°C (Charola et al., 2007). Temperatures as high as that have been recorded in 10 cm depth close to our study site, after a rain experiment when the soil moisture still reached 100%, indicating the presence of liquid water (Sager et al., 2021). Considering that these temperatures can be reached at shallow depth and that rainwater can dampen the soil at 10-30 cm depth for months (Schulze-Makuch et al., 2018; Sager et al., 2021; Jordan et al., 2020), we assume that the formation of anhydrite in the *chusca* horizon can occur through precipitation out of solar-heated water after a rain event with retention time of several months. At depths below 50 cm the temperatures remain too low for this process to occur. However, if highly soluble salts are additionally present that reduce the water activity of the solution, the formation of anhydrite can occur at lower temperatures, e.g., at 22°C in saturated sodium chloride solution based on thermodynamic calculations and laboratory experiments (Hardie, 1967; Freyer and Voigt, 2003). This causal connection between electrolyte-presence and anhydrite formation is supported by the occurrence of anhydrite in saline environments such as supratidal salt flats (sabkhas) (Wilson et al., 2013); environments that are not hyperarid but rather hot and more humid. The electrolyte-dependent anhydrite formation process is also supported by the finding of May *et al.* (2019) in other parts of the hyperarid Atacama Desert, where gypsum dominates at the surface and anhydrite in the subsurface accompanied by halite and nitratine. Hence, in the Atacama Desert, the presence of anhydrite is indirectly linked to the ambient aridity mediated through the accumulation of nitrates and chlorides in these hillslope soils, which only occurs under hyperarid conditions.

4.4. Soil habitability & Mars analogy

It is essential to understand the role that water played in assessing the habitability, which can be studied using stable isotope and mineralogical proxies. In the last two decades the habitability of the hyperarid Atacama Desert has been studied intensively showing the presence of islands of microbial communities, so-called microhabitats (e.g., Warren-Rhodes et al., 2006; Davila & Schulze-Makuch et al., 2016; Huang et al., 2020; Schulze-Makuch et al., 2021). Microhabitats near the soil surface such as hypolithic microenvironments retaining morning dew (Warren-Rhodes et al., 2006) and salt nodules attracting water vapor through hygroscopic effects, are closely linked to the ambient conditions. Schulze-Makuch *et al.* (2018) could show for the first-time microbial activity within the *chusca* horizon (in 20 - 30 cm depth) after a rain event. More challenging is the assessment of even deeper and highly cemented subsurface microenvironments where habitability is influenced by numerous and partially difficult to measure soil properties, like pore space, substrate composition, and salt concentrations at small spatial scales, in addition to water activity. Hence, if microbial activity occurs it can affect soil processes. Recent studies suggest that the plant *Helianthemum squamatum* common in Mediterranean climate (Palacio et al., 2014), and cyanobacteria collected from the Atacama Desert (Huang et al., 2020) are able to induce the liberation of the crystal water from gypsum, perhaps for their own usage. Microbial activity is likely also affecting stable isotope ratios as indicated by a soil phosphate study conducted in the Atacama Desert, which suggests that the $\delta^{18}O$ isotope ratio of phosphates can be used as a long-term proxy for microbial activity. Microbes shift the phosphate pool of the Atacama Desert soil from an authigenic bedrock to a biogenic dominated pool and thereby incorporate the $\delta^{18}O$ of the rainwater in the phosphates. However, this proxy seems to be limited to regions with >10 mm of annual water precipitation (Shen et al., 2020). In addition, the same study provided indications for microorganisms making use of the gypsum hydration water, as the phosphate $\delta^{18}O$ values were higher than the theoretical meteoric water values, which could be explained by the fractionation of water $\delta^{18}O$ during hydration of anhydrite to gypsum. Hence, it cannot be ruled out that such biologically mediated anhydrite formation also played a role in the past during more humid episodes in the here studied soils and perhaps still does.

Mars used to be home to rivers and lakes but transitioned early in its natural history into a hyperarid and cold planet (Schulze-Makuch and Irwin, 2018). During this desertification process, vast amounts of sulfates were deposited, which have been detected globally by satellite-based remote sensing (e.g., Murchie et al., 2009; Wray et al., 2010) and in-situ by the Curiosity Rover in various hydration phases (gypsum, bassanite, anhydrite) (Vaniman et al., 2018). Their formation has been proposed to have occurred at low temperatures (<50°C) in presence of highly soluble salts causing incomplete hydration during precipitation, which are very similar conditions acting on the here investigated soils in the Atacama Desert. Beyond using sulfate hydration phases as an aridity proxy, the hydration and dehydration of sulfate minerals could have served as a water reservoir for putative Martian subsurface microorganisms and may still do so. Therefore, further investigations are warranted on the usage of crystal water for microbes in analog environments and ultimately on Mars.

5. CONCLUSION

The soils along the elevation transect within the hyperarid Yungay valley, Atacama Desert, show depth-related salt separation and measured as well as modeled sulfate $\delta^{34}S$ and $\delta^{18}O$ distribution, indicating a common water-soil interaction of incomplete salt transport by infiltrating rainwater. However, the degree of soil development and the amount of soluble salts decrease with elevation, which could be a result of a higher erosion-rate with elevation controlled by steeper slopes or a change of salt input within the study area. This is also supported by the isotopic data we obtained. The investigated anhydrite occurrences at shallow depth are presumably a result of rainwater, which can remain in the soil for months, followed by slow precipitation in the shallow moist soil heated by solar radiation. Due to the lack of high temperatures at depth anhydrite can only form if highly soluble salts such as nitrates or chlorides are present. Hence, our findings are important for correctly applying the geochemical proxies for long-term environmental conditions and habitability of extremely dry soils on Earth and also for extraterrestrial analogs.

ACKNOWLEDGMENTS

The authors acknowledge the support by the European Research Council Advanced Grant Habitability Of Martian Environments (339231), which provided base funding for the study, including sample collection and laboratory analysis. Thanks to Bernardita Valenzuela and Pedro Zamorano for helping to organizing the field work. We want to thank the Mineralogy Department of the Freie Universität Berlin for providing us access to the XRD-laboratory.

REFERENCES

Amundson, R., Barnes, J.D., Ewing, S., Heimsath, A., Chong, G., 2012. The stable isotope composition of halite and sulfate of hyperarid soils and its relation to aqueous transport. Geochimica et Cosmochimica Acta 99, 271–286.

Anderson, K., Wells, S., Graham, R., 2002. Pedogenesis of vesicular horizons, Cima volcanic field, Mojave Desert, California. Soil Science Society of America Journal 66, 878–887.

Artieda, O., Davila, A., Wierzchos, J., Buhler, P., Rodríguez-Ochoa, R., Pueyo, J., Ascaso, C., 2015. Surface evolution of salt-encrusted playas under extreme and continued dryness. Earth Surf. Process. Landforms 40, 1939–1950.

Azua-Bustos, A., Fairén, A.G., González-Silva, C., Ascaso, C., Carrizo, D., Fernández-Martínez, M.Á., Fernández-Sampedro, M., García-Descalzo, L., García-Villadangos, M., Martin-Redondo, M.P., Sánchez-García, L., Wierzchos, J., Parro, V., 2018. Unprecedented rains decimate surface microbial communities in the hyperarid core of the Atacama Desert. Scientific reports 8, 16706.

Azua-Bustos, A., González-Silva, C., Corsini, G., 2017. The hyperarid core of the Atacama Desert, an extremely dry and carbon deprived habitat of potential interest for the field of carbon science. Frontiers in microbiology 8, 993.

Bozkurt, D., Rondanelli, R., Garreaud, R., Arriagada, A., 2016. Impact of warmer eastern tropical Pacific SST on the March 2015 Atacama floods. Monthly Weather Review 144, 4441–4460.

Cereceda, P., Larrain, H., Osses, P., Farías, M., Egaña, I., 2008. The spatial and temporal variability of fog and its relation to fog oases in the Atacama Desert, Chile. Atmospheric Research 87, 312–323.

Charola, A.E., Pühringer, J., Steiger, M., 2007. Gypsum: a review of its role in the deterioration of building materials. Environ Geol 52, 339–352.

Criss, R.E., 1999. Principles of stable isotope distribution. Oxford University Press on Demand.

Davila, A.F., Schulze-Makuch, D., 2016. The last possible outposts for life on Mars. Astrobiology 16, 159–168.

Ericksen, G.E., 1981. Geology and origin of nitrate deposition in Atacama Desert. Geological Survey Professional Paper 1188.

Ewing, S.A., Michalski, G., Thiemens, M., Quinn, R.C., Macalady, J.L., Kohl, S., Wankel, S.D., Kendall, C., McKay, C.P., Amundson, R., 2007. Rainfall limit of the N cycle on Earth. Global Biogeochem. Cycles 21, 1-12.

Ewing, S.A., Sutter, B., Owen, J., Nishiizumi, K., Sharp, W., Cliff, S.S., Perry, K., Dietrich, W., McKay, C.P., Amundson, R., 2006. A threshold in soil formation at Earth's arid–hyperarid transition. Geochimica et Cosmochimica Acta 70, 5293–5322.

Ewing, S.A., Yang, W., DePaolo, D.J., Michalski, G., Kendall, C., Stewart, B.W., Thiemens, M., Amundson, R., 2008. Non-biological fractionation of stable Ca isotopes in soils of the Atacama Desert, Chile. Geochimica et Cosmochimica Acta 72, 1096–1110.

Finstad, K., Pfeiffer, M., McNicol, G., Barnes, J., Demergasso, C., Chong, G., Amundson, R., 2016. Rates and geochemical processes of soil and salt crust formation in Salars of the Atacama Desert, Chile. Geoderma 284, 57–72.

Freyer, D., Voigt, W., 2003. Crystallization and phase stability of CaSO 4 and CaSO 4 - based salts. Monatshefte für Chemie / Chemical Monthly 134, 693–719.

Hardie, A.L., 1967. The gypsum-anhydrite equilibrium at one atmosphere pressure. American Mineralogist 52, 171–200.

Houston, J., Hartley, A.J., 2003. The central Andean west-slope rainshadow and its potential contribution to the origin of hyper-aridity in the Atacama Desert. Int. J. Climatol. 23, 1453–1464.

Huang, W., Ertekin, E., Wang, T., Cruz, L., Dailey, M., DiRuggiero, J., Kisailus, D., 2020. Mechanism of water extraction from gypsum rock by desert colonizing microorganisms. Proceedings of the National Academy of Sciences 117, 10681–10687.

Jordan, T., Riquelme, R., González, G., Herrera, C., Godfrey, L., Colucci, S., Gironás-León, J., Gamboa, C., Urrutia, J., Tapia, L., others, 2015. Hydrological and geomorphological consequences of the extreme precipitation event of 24-26 March 2015, Chile, in: XIV Congreso Geológico de Chile.

Jordan, T.E., Kirk-Lawlor, N.E., Blanco, N.P., Rech, J.A., Cosentino, N.J., 2014. Landscape modification in response to repeated onset of hyperarid paleoclimate states since 14 Ma, Atacama Desert, Chile. Geological Society of America Bulletin 126, 1016–1046.

Jordan, T.E., Lohman, R.B., Tapia, L., Pfeiffer, M., Scott, C.P., Amundson, R., Godfrey, L., Riquelme, R., 2020. Surface materials and landforms as controls on InSAR permanent and transient responses to precipitation events in a hyperarid desert, Chile. Remote Sensing of Environment 237, 111544.

Lloyd, R.M., 1968. Oxygen isotope behavior in the sulfate-water system. J. Geophys. Res. 73, 6099–6110.

May, S.M., Hoffmeister, D., Wolf, D., Bubenzer, O., 2019. Zebra stripes in the Atacama Desert revisited – Granular fingering as a mechanism for zebra stripe formation? Geomorphology 344, 46–59.

McFadden, L.D., McDonald, E.V., Wells, S.G., Anderson, K., Quade, J., Forman, S.L., 1998. The vesicular layer and carbonate collars of desert soils and pavements: formation, age and relation to climate change. Geomorphology, 101–145.

McKay, C.P., Friedmann, E.I., Gómez-Silva, B., Cáceres-Villanueva, L., Andersen, D.T., Landheim, R., 2003. Temperature and Moisture Conditions for Life in the Extreme Arid Region of the Atacama Desert: Four Years of Observations Including the El Niño of 1997–1998. Astrobiology.

Michalski, G., Böhlke, J.K., Thiemens, M., 2004. Long term atmospheric deposition as the source of nitrate and other salts in the Atacama Desert, Chile: New evidence from mass-independent oxygen isotopic compositions. Geochimica et Cosmochimica Acta 68, 4023–4038.

Murchie, S.L., Mustard, J.F., Ehlmann, B.L., Milliken, R.E., Bishop, J.L., McKeown, N.K., Noe Dobrea, E.Z., Seelos, F.P., Buczkowski, D.L., Wiseman, S.M., Arvidson, R.E., Wray, J.J., Swayze, G., Clark, R.N., Des Marais, D.J., McEwen, A.S., Bibring, J.-P., 2009. A synthesis of Martian aqueous mineralogy after 1 Mars year of observations from the Mars Reconnaissance Orbiter. J. Geophys. Res. 114, 711.

Owen, J.J., Dietrich, W.E., Nishiizumi, K., Chong, G., Amundson, R., 2013. Zebra stripes in the Atacama Desert: Fossil evidence of overland flow. Geomorphology 182, 157–172.

Palacio, S., Azorín, J., Montserrat-Martí, G., Ferrio, J.P., 2014. The crystallization water of gypsum rocks is a relevant water source for plants. Nature communications 5, 4660.

Pérez-Fodich, A., Reich, M., Álvarez, F., Snyder, G.T., Schoenberg, R., Vargas, G., Muramatsu, Y., Fehn, U., 2014. Climate change and tectonic uplift triggered the formation of the Atacama Desert’s giant nitrate deposits. Geology 42, 251–254.

Pfeiffer, M., Morgan, A., Heimsath, A., Jordan, T., Howard, A., Amundson, R., 2021. Century scale rainfall in the absolute Atacama Desert: Landscape response and implications for past and future rainfall. Quaternary Science Reviews 254, 106797.

Placzek, C.J., Matmon, A., Granger, D.E., Quade, J., Niedermann, S., 2010. Evidence for active landscape evolution in the hyperarid Atacama from multiple terrestrial cosmogenic nuclides. Earth and Planetary Science Letters 295, 12–20.

Quade, J., Reiners, P., Placzek, C., Matmon, A., Pepper, M., Ojha, L., Murray, K., 2012. Seismicity and the strange rubbing boulders of the Atacama Desert, northern Chile. Geology 40, 851–854.

Rech, J.A., Quade, J., Hart, W.S., 2003. Isotopic evidence for the source of Ca and S in soil gypsum, anhydrite and calcite in the Atacama Desert, Chile. Geochimica et Cosmochimica Acta 67, 575–586.

Ritterbach, L., Becker, P., 2020. Temperature and humidity dependent formation of CaSO4xH2O (x= 0… 2) phases. Global and Planetary Change 187, 103132.

Sager, C., Airo, A., Arens, F.L., Rabethge, C., Schulze-Makuch, D., 2020. New types of boulder accumulations in the hyper-arid Atacama Desert. Geomorphology 350, 106897.

Sager, C., Airo, A., Arens, F.L., Schulze-Makuch, D., 2021. New type of sand wedge polygons in the salt cemented soils of the hyper-arid Atacama Desert. Geomorphology 373, 107481.

Schulze-Makuch, D., Irwin, L.N., 2018. Life in the Universe: Expectations and Constraints, 3rd ed. Springer International Publishing, Cham, 343 pp.

Schulze-Makuch, D., Wagner, D., Kounaves, S.P., Mangelsdorf, K., Devine, K.G., Vera, J.-P. de, Schmitt-Kopplin, P., Grossart, H.-P., Parro, V., Kaupenjohann, M., Galy, A., Schneider, B., Airo, A., Frösler, J., Davila, A.F., Arens, F.L., Cáceres, L., Cornejo, F.S., Carrizo, D., Dartnell, L., DiRuggiero, J., Flury, M., Ganzert, L., Gessner, M.O., Grathwohl, P., Guan, L., Heinz, J., Hess, M., Keppler, F., Maus, D., McKay, C.P., Meckenstock, R.U., Montgomery, W., Oberlin, E.A., Probst, A.J., Sáenz, J.S., Sattler, T., Schirmack, J., Sephton, M.A., Schloter, M., Uhl, J., Valenzuela, B., Vestergaard, G., Wörmer, L., Zamorano, P., 2018. Transitory microbial habitat in the hyperarid Atacama Desert. Proceedings of the National Academy of Sciences of the United States of America 115, 2670–2675.

Schulze-Makuch, D., Lipus, D., Arens, F.L., Baqué, M., Bornemann, T.L.V., deVera, JP., Flury, M., Frösler, J., Heinz, J., Hwang, Y., Kounaves, S.P., Kai Mangelsdorf11, Meckenstock, R.U., Pannekens, M., Probst, A.J., Sáenz J.S., Schirmack, J., Schloter, M., Schmitt-Kopplin, P., Schneider, B., Uhl, J., Vestergaard, G., Valenzuela, B., Zamorano, P., Wagner, D. 2021. Lithic Microhabitats and Microbial hotspots in the Atacama Desert inferred from DNA fractionation and metagenomics. Microorganisms 9, 1038.

Seal, R.R., Alpers, C.N., Rye, R.O., 2000. Stable isotope systematics of sulfate minerals. Reviews in Mineralogy and Geochemistry 40, 541–602.

Seufert, S., Hesse, C., Götz-Neunhoeffer, F., Neubauer, J., 2009. Discrimination of bassanite and anhydrite III dehydrated from gypsum at different temperatures. Zeitschrift für Kristallographie, Supplement Suppl. 30, 447–452.

Shen, J., Smith, A.C., Claire, M.W., Zerkle, A.L., 2020. Unraveling biogeochemical phosphorus dynamics in hyperarid Mars-analogue soils using stable oxygen isotopes in phosphate. Geobiology 18, 760–779.

Sutter, B., Dalton, J.B., Ewing, S.A., Amundson, R., McKay, C.P., et al., 2007. Terrestrial analogs for interpretation of infrared spectra from the Martian surface and subsurface: Sulfate, nitrate, carbonate, and phyllosilicate-bearing Atacama Desert soils. Journal of Geophysical Research 112.

van Driessche, A.E.S., Canals, A., Ossorio, M., Reyes, R.C., Garcia-Ruiz, J.M., 2016. Unraveling the sulfate sources of (giant) gypsum crystals using gypsum isotope fractionation factors. The Journal of Geology 124, 235–245.

Vaniman, D.T., Martínez, G.M., Rampe, E.B., Bristow, T.F., Blake, D.F., Yen, A.S., Ming, D.W., Rapin, W., Meslin, P.-Y., Morookian, J.M., Downs, R.T., Chipera, S.J., Morris, R.V., Morrison, S.M., Treiman, A.H., Achilles, C.N., Robertson, K., Grotzinger, J.P., Hazen, R.M., Wiens, R.C., Sumner, D.Y., 2018. Gypsum, bassanite, and anhydrite at Gale crater, Mars. American Mineralogist 103, 1011–1020.

Voigt, C., Klipsch, S., Herwartz, D., Chong, G., Staubwasser, M., 2020. The spatial distribution of soluble salts in the surface soil of the Atacama Desert and their relationship to hyperaridity. Global and Planetary Change 184, 103077.

Warren-Rhodes, K.A., Rhodes, K.L., Pointing, S.B., Ewing, S.A., Lacap, D.C., Gómez-Silva, B., Amundson, R., Friedmann, E.I., McKay, C.P., 2006. Hypolithic cyanobacteria, dry limit of photosynthesis, and microbial ecology in the hyperarid Atacama Desert. Microbial ecology, 389–398.

Wilhelm, M.B., Davila, A.F., Eigenbrode, E.S., Parenteau, M.N., Liu, X., Summons, R.E., Wray, J.J., Stamos, B.N., O`Reilly, S.S., Williams, A., 2017. Xeropreservation of functionalized lipid biomarkers in hyperarid soils in the Atacama Desert. Organic Chemistry 103.

Wilson, M.A., Shahid, S.A., Abdelfattah, M.A., Kelley, J.A., Thomas, J.E., 2012. Anhydrite Formation on the Coastal Sabkha of Abu Dhabi, United Arab Emirates. In: Shahid, S.A., Taha, F.K., Abdelfattah, M.A. (Eds.) Developments in Soil Classification, Land Use Planning and Policy Implications. Innovative Thinking of Soil Inventory for Land Use Planning and Management of Land Resources. Springer, Dordrecht, pp. 175–201.

Wray, J.J., Squyres, S.W., Roach, L.H., Bishop, J.L., Mustard, J.F., Noe Dobrea, E.Z., 2010. Identification of the Ca-sulfate bassanite in Mawrth Vallis, Mars. Icarus 209, 416–421.

Zeebe, R.E., 2010. A new value for the stable oxygen isotope fractionation between dissolved sulfate ion and water. Geochimica et Cosmochimica Acta 74, 818–828.

Supplements

for

Geochemical proxies for water-soil interactions in the hyperarid Atacama Desert, Chile

Table S1 Whole soil values

	Location				Weighted average values		Total salt inventory		
Soil profile	Longitude	Latitude	Elevation	Slope	$\delta^{34}S_{VCDT}$	$\delta^{18}O_{SMOW}$	SO_4^{2-}	Cl^-	NO_3^-
	[WGS84]		[m a.s.l.]	[°]	[‰]	[‰]		[kg m^{-2}]	
HP	24°03’47”S	70°01’06”W	1436	8	7.6	3.0	256	0.04	0.18
HM	24°04’17”S	70°03’08”W	1217	6	6.8	2.0	325	2.45	0.37
HD	24°05’18”S	69°59’40”W	1005	2	5.3	5.5	395	5.99	7.64
TD	24°06’06”S	70°01’06”W	1021	1	3.7[a]	7.5[a]	240[b]	62.9 [b]	6.47 [b]

[a] value based on data from Ewing *et al.*, (2008)
[b] for total salt inventory of TD only values <140 cm depth are considered.

Table S2 All quantified analytical results

Sample	Sample interval	δ^{34}S[a] measured	δ^{34}S modeled	δ^{18}O[b] measured	δ^{18}O modeled	SO_4^{2-}[c]	Cl^-[c]	NO_3^-[c]	Soluble content[d]
	[cm]			[‰]			[mg g^{-1}]		[wt%]
Herradura Proximal (HP)									
HP-0	0-5	12.1	9.6	11.0	6.3	28.4	0.0	0.0	10
HP-10	5-15	9.6	9.3	6.2	5.8	582	0.0	0.0	83
HP-20	15-25	9.1	8.8	6.5	5.1	357	0.0	0.0	49
HP-30	25-35	7.0	8.4	2.9	3.8	357	0.0	0.3	46
HP-40	35-45	6.8	7.7			276	0.0	0.2	34
HP-50	45-55					275	0.0	0.1	32
HP-60	55-65	5.9	6.1	-0.7	0.8	436	0.0	0.2	54
HP-70	65-75					130	0.0	0.3	15
HP-80	75-85	5.8	3.1	-1.0	-4.5	96.6	0.3	0.4	5
HP-90	85-95	6.5	-1.0	1.0	-11.3	67.3	0.2	0.4	12
Herradura Medial (HM)									
HM-0	0-2.5	10.2	8.8	9.3	5.3	0.25	0.00	0.00	2
HM-5	2.5-7.5	8.3	8.8	5.6	5.3				
HM-10	7.5-15	8.0	8.8	3.8	5.3	0.19	0.00	0.00	1
HM-20	15-25	8.7	8.7	5.1	5.1	324	0.00	0.00	50
HM-30	25-35	7.7	8.5	3.7	4.7	405	0.00	0.00	52
HM-40	35-45	6.4	8.0	1.1	4.0	410	0.00	0.00	54
HM-50	45-55					394	0.00	0.00	53
HM-60	55-65	6.1	7.2	0.4	2.5	518	0.00	0.00	54
HM-70	65-75					425	0.33	0.00	39
HM-80	75-85	6.8	5.2	2.2	-0.7	423	3.38	0.95	33
HM-90	85-95					343	20.8	2.73	50
HM-100	95-105	6.6	1.0	1.9	-7.5	18.8	0.07	0.00	6
Herradura Distal (HD)									
HD-0	0-2.5	8.0	7.3	9.7	8.8	26.2	0.00	0.00	1
HD-5	2.5-7.5	7.8	7.2	8.6	8.7	539	0.00	0.00	79
HD-10	7.5-15	6.5	7.1	6.3	8.4	509	0.00	0.00	84
HD-20	15-25	5.3	6.8	4.7	8.1	388	0.00	0.00	71
HD-30	25-35	6.0	6.6	5.9	7.6	416	0.00	0.00	74
HD-40	35-45	4.3	6.0	2.8	6.8	556	0.11	0.08	82
HD-50	45-55					447	1.57	0.57	68
HD-60	55-65	5.1	5.4	5.7	5.7	70.6	3.30	2.46	16
HD-70	65-75					84.8	3.95	1.78	19

Sample	Sample interval	$\delta^{34}S$[a] measured	$\delta^{34}S$ modeled	$\delta^{18}O$[b] measured	$\delta^{18}O$ modeled	SO_4^{2-} [c]	Cl^- [c]	NO_3^- [c]	Soluble content[d]
	[cm]			[‰]			[mg g^{-1}]		[wt%]
HD-80	75-85	5.2	5.0	5.5	5.1	114	5.56	1.99	18
HD-90	85-95					54.7	1.89	1.41	11
HD-100	95-105	5.1	4.6	6.1	4.5	59.4	2.31	2.63	15
HD-110	105-115					273	2.49	2.77	42
HD-120	115-125	5.4	3.9	6.5	3.2	233	1.61	2.37	42
HD-130	125-135					104	6.48	6.26	17
HD-140	135-145	4.8	2.7	6.4	1.2	107	4.67	6.08	13
HD-150	145-155					207	6.06	15.9	60
HD-160	155-165	3.8	-0.1	7.1	-3.3	355	39.9	64.3	58
Tetas Distal (TD)									
TD-0	0-2.5					6.98	0.00	0.00	4
TD-1	*0-2.5*	*9.6*	5.7	*13*	10.8	*77*			
TD-2.5	*2-3*	*9.2*	5.7	*11*	10.8	*384*			
TD-5	2.5-7.5					686	0.00	0.00	61
TD-7.5	*3-12*	*6.9*	5.6	*10*	10.6	*240*			
TD-10	7.5-15					448	0.00	0.00	57
TD-19	*12-26*	*4*	5.4	*9*	10.2	*269*			
TD-20	15-25	4.3		7.0		211	0.00	0.00	46
TD-30	25-35					326	0.00	0.00	27
TD-32.5	*26-39*	*5*	5	*8*	9.6	*288*			
TD-40	35-45					248	0.75	0.34	34
TD-50	45-55					142	4.67	1.62	25
TD-55	*39-71*	*4.3*	4.2	*7*	8.3	*221*			
TD-60	55-65					15	4.41	1.61	29
TD-70	65-75					133	34.7	4.97	29
TD-78.5	*71-85*	*2.2*	3.2	*8*	6.6	*192*			
TD-80	75-85					63.7	8.69	3.77	13
TD-90	85-95					93.6	9.29	12.6	27
TD-94	*85-102*	*1.4*	2.2	*5*	4.9	*182*			
TD-100	95-105					131	29.7	4.94	29
TD-110	105-115					92.2	85.6	7.60	39
TD-112	*102-122*	*0.8*	-0.7	*6*	0.3	*144*			
TD-120	115-125					79.6	7.75	12.3	22
TD-130	125-135					17.2	438	9.94	81
TD-140	135-145					57.3	8.22	10.2	17
TD-150	145-155					57.8	5.43	10.4	20
TD-160	155-165					57.2	2.69	3.75	18
TD-170	165-175					29.3	1.40	1.36	15
TD-180	175-185					50.2	2.45	3.40	18
TD-190	185-195					60.4	1.88	4.43	21
TD-200	195-205					51.6	3.06	4.86	17

[a] Uncertainty is ±0.3‰

[b] Uncertainty is ±0.6‰

[c] Uncertainty is 10%

[d] Uncertainty is 5%

Data & values from Ewing *et al.* (2008) are in *italic and underlined*

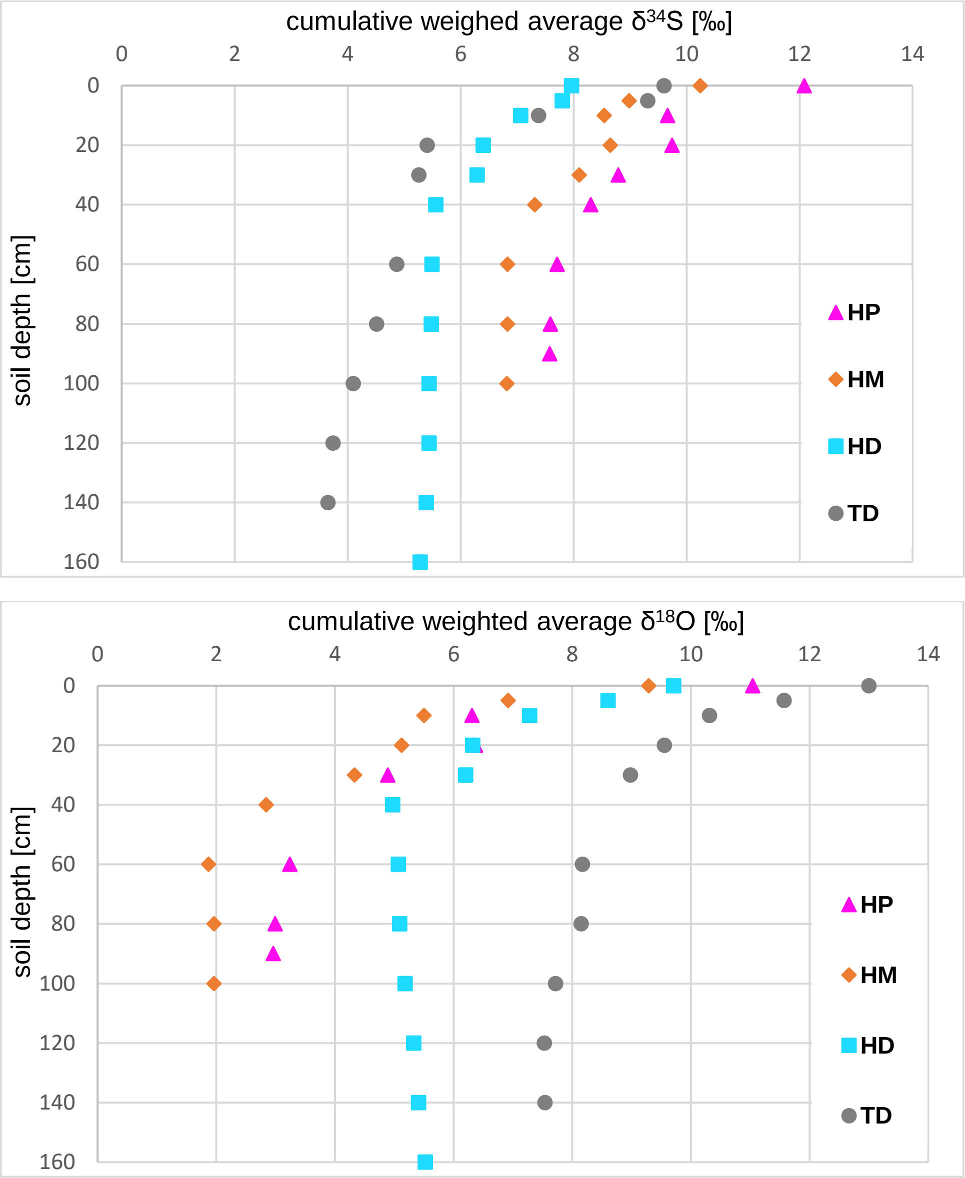

Figure S1 cumulative weighted average of δ^{34}S and δ^{18}O for each soil profile considering different maximum soil depth.

HERRADURA PROXIMAL

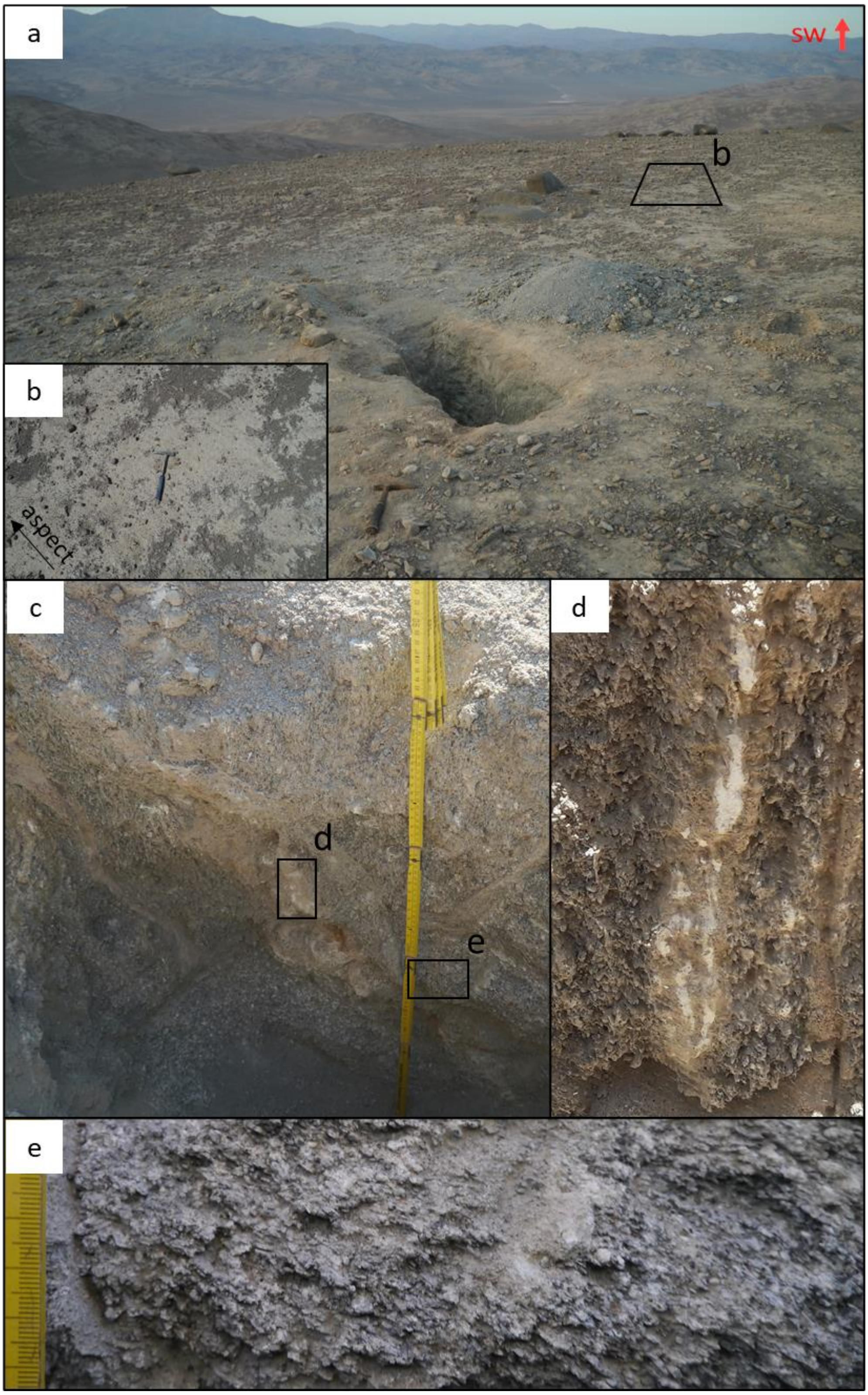

Figure S2 Herradura Proximal site. a) The pit is located near the crest of Cerro Herradura, in the vicinity weathered bedrock core-stones on the surface are present. b) Loose surface clasts, lying on a clay-rich crust, have sorted in hillslope-parallel bands, described by Owen et al. (2013) as a result of overland-flow or due to seismic shaking by May et al. (2019). c) Overview of the soil profile. Prominent filled crack/veins (d) cut through the matrix of fragmented bedrock (e). These veins are filled by salt (sulfate) and silicate dust. The bedrock, fragmented into clasts of few mm size, is coated in salt.

HERRADURA MEDIAL

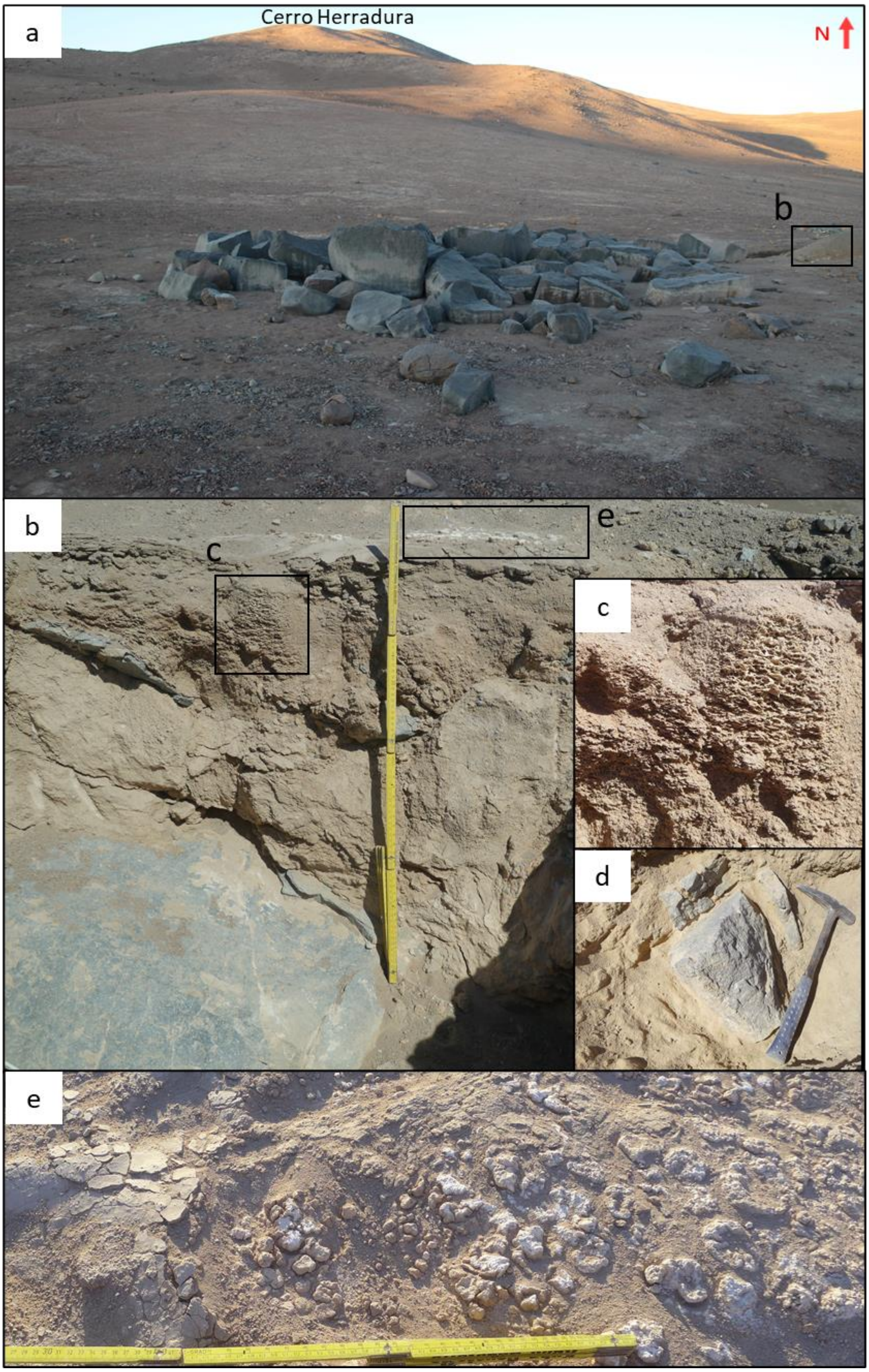

Figure S3 Herradura Medial site. a) The pit is located 1.4 km downslope of Cerro Herradura, near a boulder cluster (described by Sager et al. 2020). b) The soil profile is situated on an intrusive dyke, being more weathering resistant than the surrounding bedrock. The dyke material is fractured by salt (d) and is floating in the soil matrix, which is highly cemented by sulfates. In the upper soil layer (~10-20cm depth) lies the vesicular layer (c) with its typical porous sponge-like texture. e) Above lies a weakly cemented clay-rich layer, covered by a desert pavement. In areas where the vesicular layer is close to the surface initial losas are present.

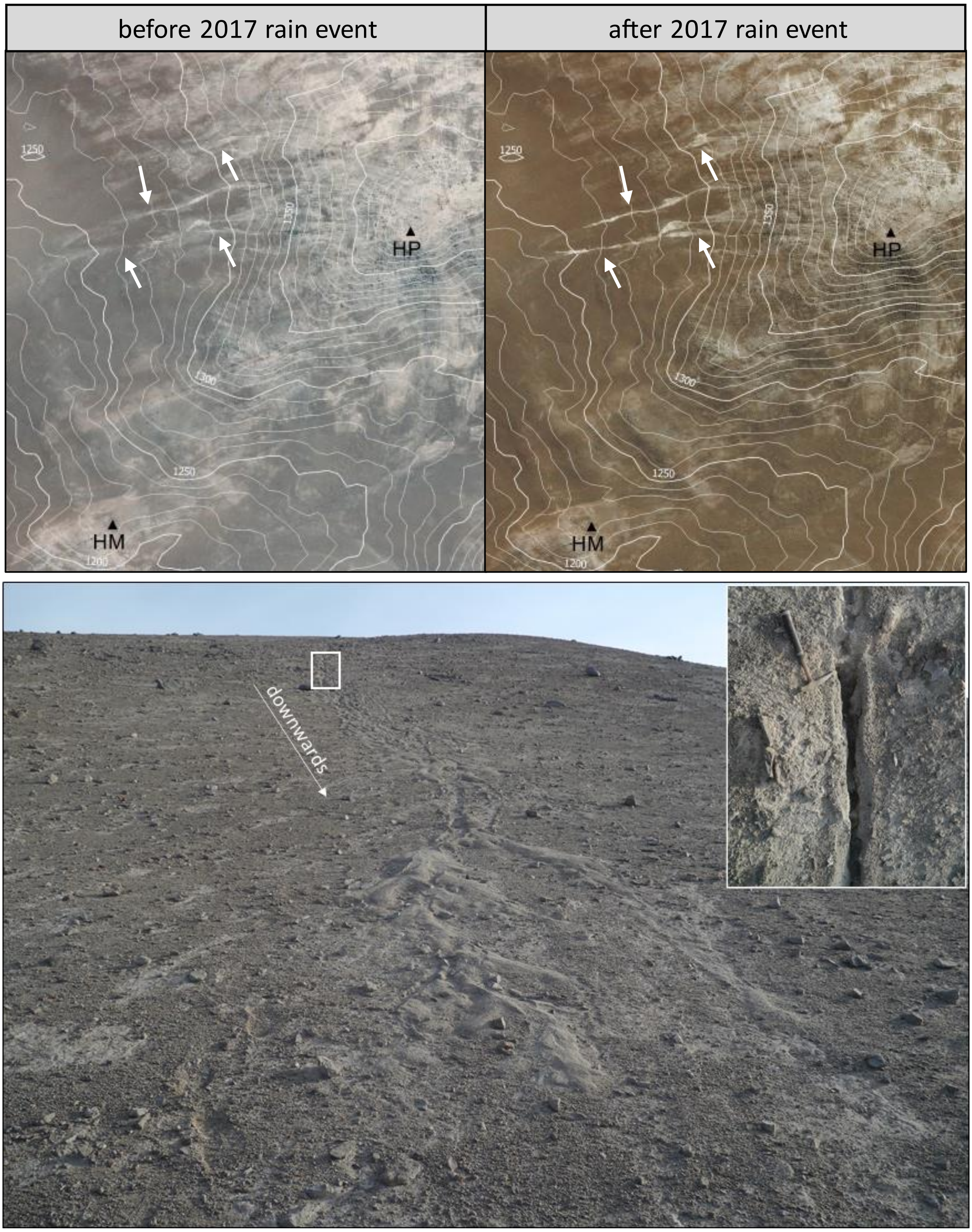

before 2017 rain event

after 2017 rain event

Figure S4 surface run-off tracks after the rain event in 2017 in the study area recorded by us and other research group e.g. Jordan et al. (2020). Upper two images are satellite data based (visual (from Bing Maps, Microsoft 2016 & 2019) and STRM), showing the Cerro Herradura mountain with the two pits HP and HD and elevation contour lines. On the west slope fresh surface run-off channels are visible after the rain event, marked with white arrow. Lower image shows field observation of the run-off channel. Inlet image shows channel further upslope.

HERRADURA DISTAL

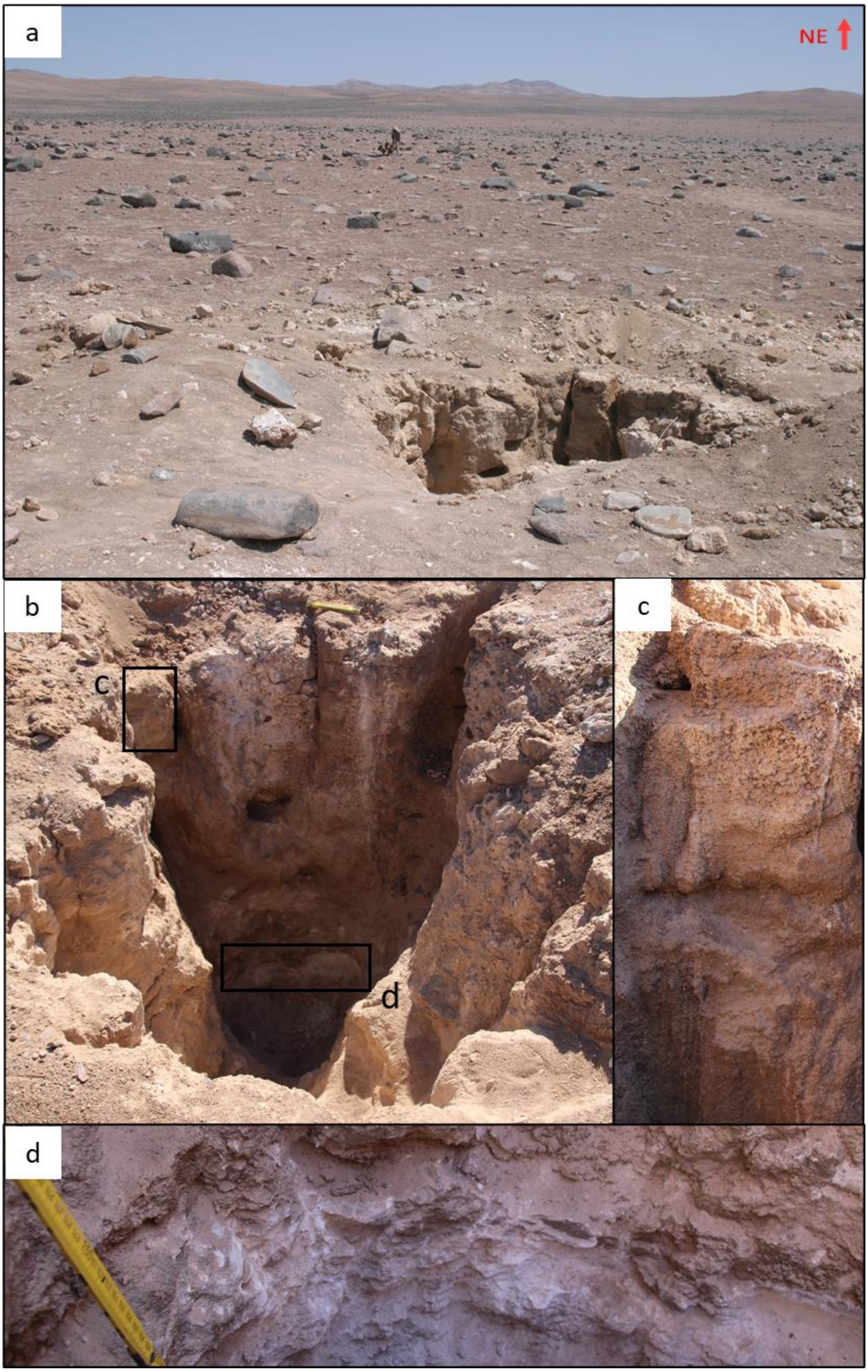

Figure S5 Herradura Distal site. a) The pit with surrounding alluvial fan area, covered with boulders. b) Overview of the soil column, separated by vertical layered sand-wedges (c). Well-developed chuca horizon (including vesicular layer) grading into costra with pebble- and cobble-size clasts floating is a firmly cemented fine-grain matrix. Due to the excavation the surface soil horizon (chuca) was removed on the opposing sidewall exposing the costra. In the base of the soil firmly cemented nitrate-rich caliche (d) is present.

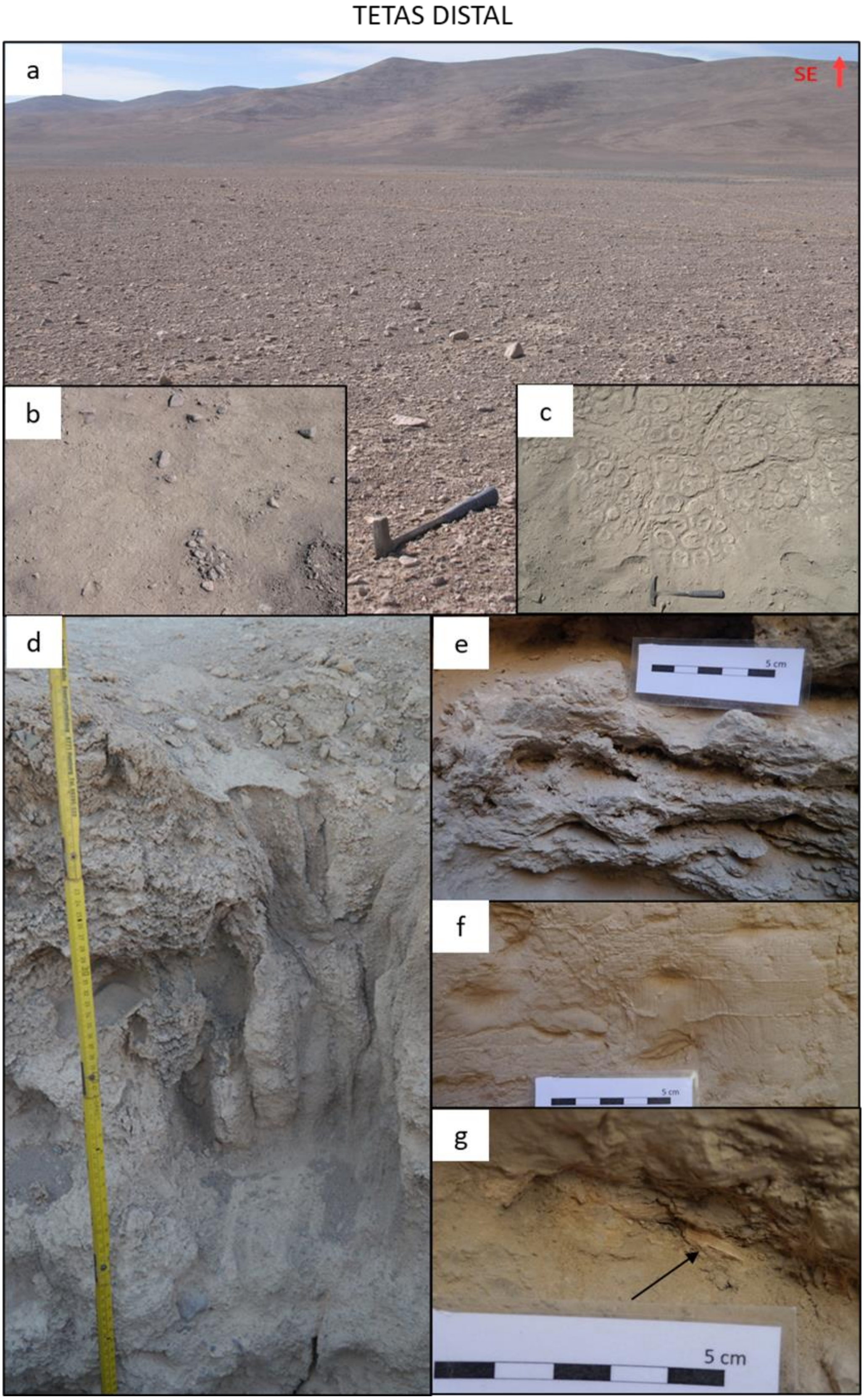

Figure S6 Tetas Distal site. a) It is located on the southern side of the valley with smooth alluvial fan, without boulder cover and a well-developed desert pavement. b) By removing the loose surface clasts, a clay-rich crust appears. c) When removing the clay crust the losa (Fig. S6) emerge in patches separated by sand-wedges. (d) Upper soil is similar to the Herradura Distal. With increasing soil depth, the maximum clasts-size decreases. At 130 cm depth a chloride-rich horizon with cavities is present. (f) Below silt and clay dominate the lithic fraction, deposited in fine layers, which are cut by a fine grid of salt veins. Within this matrix plant fragments (g) are embedded.

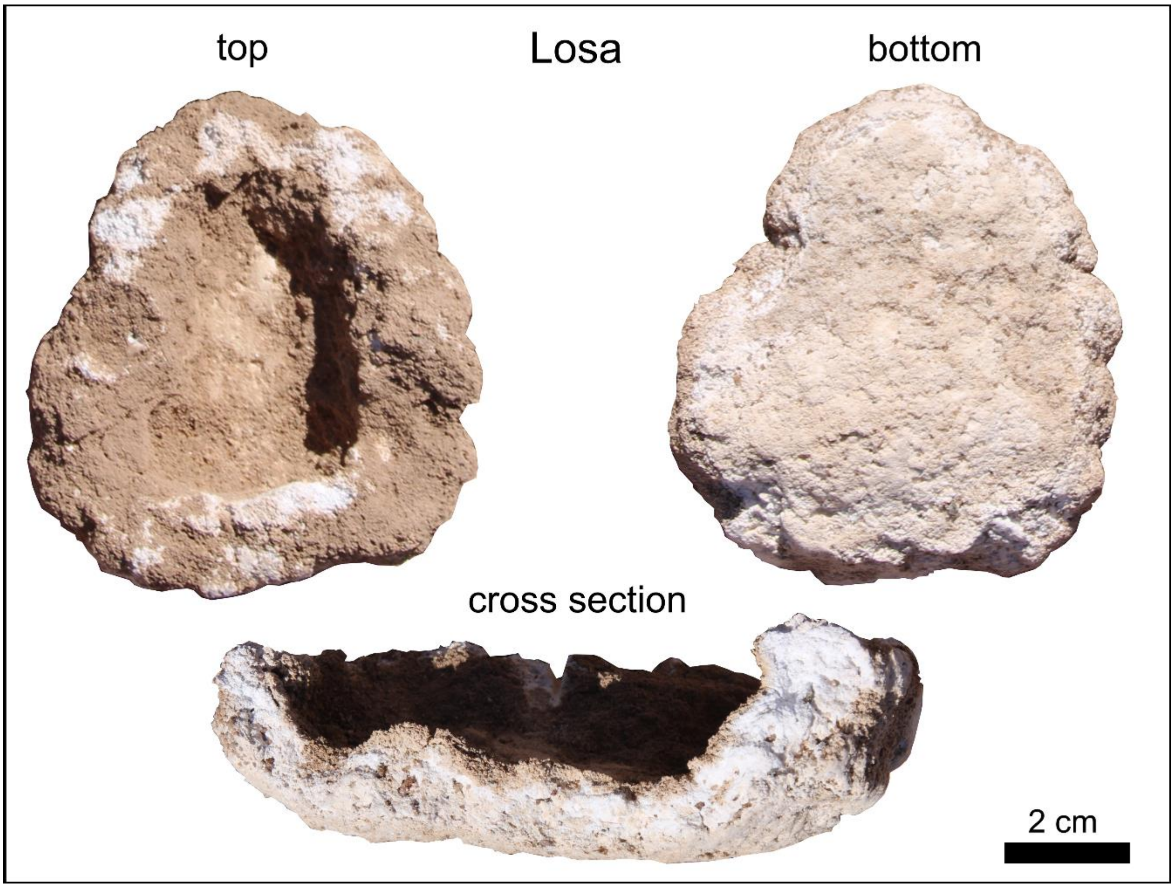

Figure S7 losa, bowl-shaped cakes. The two exemplars (1. in top & bottom view and 2. in cross section view) were excavated near HD and the loose topsoil, consisting of sand and dust particles was removed.

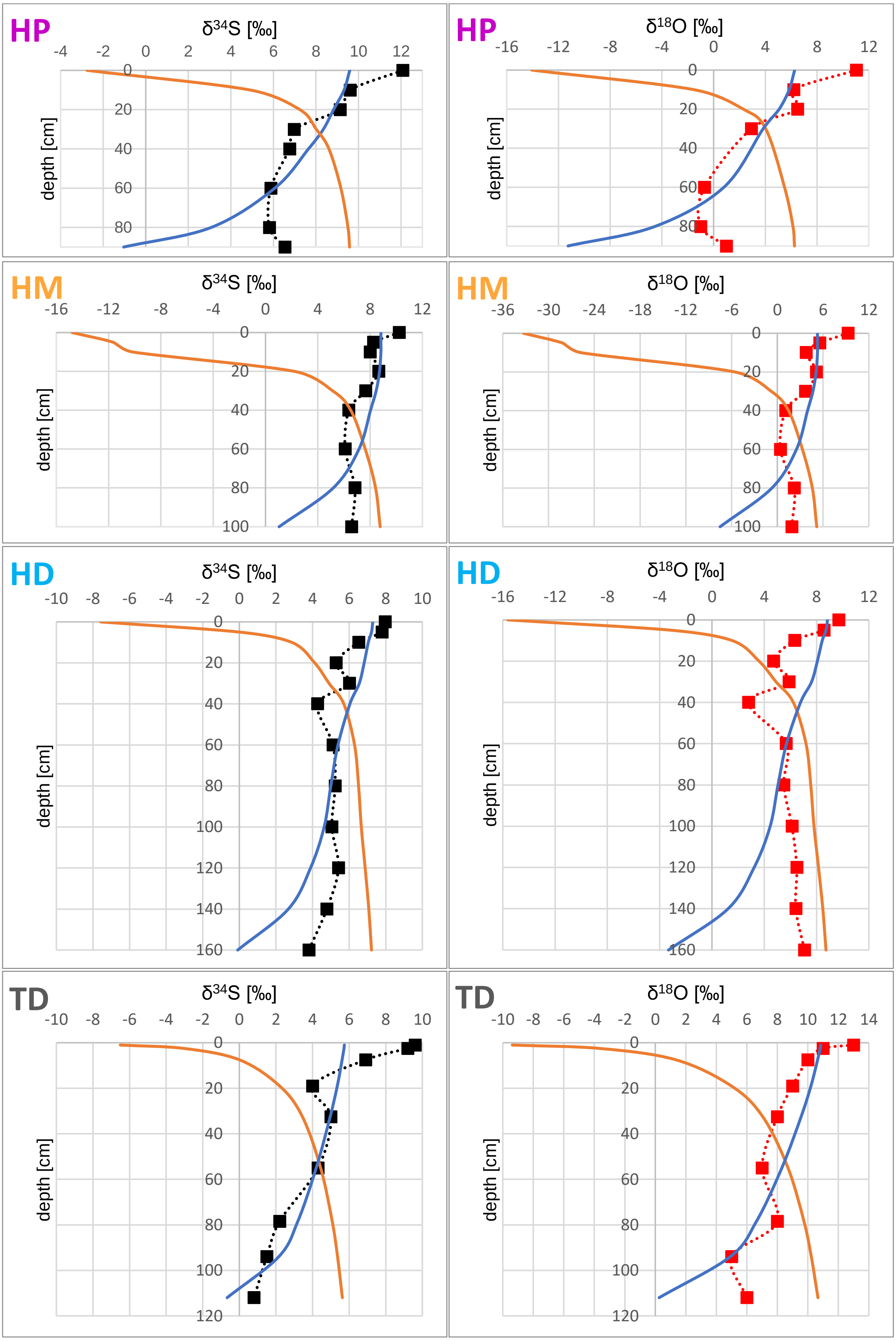

Figure S8 Rayleigh model for $\delta^{34}S$ (black, dotted) and $\delta^{18}O$ (red, dotted) of each profile. Blue curve results in modeling a downward water flow from top to bottom and the orange curve results in modeling the inverse, upward water flow from bottom to top.